

Charge transfer stabilization of late transition metal oxide nanoparticles on a layered niobate support

Megan E. Strayer,¹ Thomas P. Senftle,² Jonathan P. Winterstein,³ Nella M. Vargas-Barbosa,¹ Renu Sharma,³ Robert M. Rioux,^{1,2} Michael J. Janik,^{*2} and Thomas E. Mallouk^{*1}

¹Departments of Chemistry, Physics and Biochemistry and Molecular Biology and ²Department of Chemical Engineering, The Pennsylvania State University, University Park, Pennsylvania 16802, United States

³Center for Nanoscale Science and Technology, National Institute of Standards and Technology, Gaithersburg, Maryland 20899, United States

ABSTRACT: The interfacial interactions between late transition metal/metal oxide nanoparticles and oxide supports impact catalysts' activity and stability. Here, we report the use of isothermal titration calorimetry (ITC), electron microscopy and density functional theory (DFT) to explore periodic trends in the heats of nanoparticle-support interactions for late transition metal and metal oxide nanoparticles on layered niobate and silicate supports. Data for Co(OH)₂, hydroxyiridate-capped IrO_xnH₂O, Ni(OH)₂, CuO, and Ag₂O nanoparticles were added to previously reported data for Rh(OH)₃ grown on nanosheets of TBA_{0.24}H_{0.76}Ca₂Nb₃O₁₀ and a layered silicate. ITC measurements showed stronger bonding energies in the order Ag < Cu ≈ Ni ≈ Co < Rh < Ir on the niobate support, as expected from trends in M-O bond energies. Nanoparticles with exothermic heats of interaction were stabilized against sintering as revealed by temperature resolved images recorded using transmission electron microscopy. In contrast, ITC measurements showed endothermic interactions of Cu, Ni, and Rh oxide/hydroxide nanoparticles with the silicate and poor resistance to sintering. These trends in interfacial energies were corroborated by DFT calculations using single-atom and four-atom cluster models of surface-bound metal/metal oxide nanoparticles. Density of states and charge density difference calculations reveal that strongly bonded metals (Rh, Ir) transfer d-electron density from the adsorbed cluster to niobium atoms in the support; this mixing is absent in weakly binding metals, such as Ag and Au, and in all metals on the layered silicate support. The large differences between the behavior of nanoparticles on niobate and silicate supports highlight the importance of d-orbital interactions between the nanoparticle and support in controlling the nanoparticles' stability.

Introduction

Late transition metal nanoparticles dispersed on high surface area oxide supports are essential to technologies in the energy, chemical, and environmental industries, where they are employed as catalysts and electrocatalysts. The activity and selectivity of these catalysts are dependent on the size¹⁻⁸ and shape⁹ of the active nanoparticles, the composition of the oxide support,^{1-5,10} and the extent of support reduction.^{4,5,11-15} Therefore, the interfacial interactions between catalytic nanoparticles and supports are key parameters in determining catalyst stability, activity and selectivity.

Under catalytic reaction conditions, nanoparticles can grow to form larger, less active particles. The rate and extent of particle growth is controlled in large measure by the details of the nanoparticle/support interface. Both theoretical¹⁶⁻²⁰ and experimental studies^{4,21-25} have investigated the atomic-level structure of this interface. Although nanoparticle-support interactions are clearly implicated in the migration of particles leading to coalescence and in the kinetics of Ost-

wald ripening, there is still relatively little direct experimental quantification of the bonding at the nanoparticle-support interface.^{4,26}

To understand these interactions, Campbell and coworkers have recently measured the enthalpy of interfacial bonding using a piezoelectric metal adsorption calorimeter.²⁷ Atoms of elemental Ag, Cu, Ca, Li, and Pb were vapor deposited onto single crystal oxide supports, including MgO, CeO₂ and Fe₃O₄. The heat of interaction was found to be strongly dependent on both the nanoparticle size and support composition (reference 4 and references within).

More recently, we reported the use of solution-based isothermal titration calorimetry (ITC) to quantify the heat of interaction between rhodium hydroxide nanoparticles and several early transition metal oxide and main group oxide supports.²⁶ These heats were also found to be strongly dependent on the oxide support composition. Stronger interfacial bonding was found to inhibit nanoparticle sintering in vacuum and under reducing atmospheres at elevated temperatures. Rhodium hydroxide nanoparticles bond exothermi-

cally to early transition metal (niobium, tantalum, and tungsten) oxide supports, which inhibit nanoparticle sintering. Conversely, the interfacial bonding to main group oxide supports, such as silica and alumina, is endothermic and particle growth on these oxides occurs at a much lower temperature.²⁶

In the present study, we combine calorimetric measurements with density functional theory (DFT) calculations to map out the periodic trends in the strength of the nanoparticle-support interaction and to understand the reason for the anomalously strong bonding of late transition metals to early transition metal oxides. ITC was used to quantify the heats of interaction of cobalt, iridium, nickel, copper and silver metal oxide/hydroxide nanoparticles to a layered niobium oxide support and compared to a high surface area silicon oxide support. In situ high-resolution transmission electron microscopy (HRTEM) and high-angle annular dark field scanning transmission electron microscopy (HAADF STEM) were used to track the sintering of nanoparticles as a function of temperature under vacuum. A clear correlation between the strength of interfacial bonding and the resistance of nanoparticles to growth in vacuum was observed. DFT calculations of model systems were consistent with the experimental data and provided insight into the nature of charge transfer interactions that strongly stabilize late transition metal/metal oxide nanoparticles on early transition metal oxide supports.

Materials and Methods

Supported nanoparticle synthesis. The layered oxide $\text{KCa}_2\text{Nb}_3\text{O}_{10}$ was synthesized as previously reported.²⁸ Briefly, a 0.4 mol/mol (mole fraction) stoichiometric excess of K_2CO_3 was ground with stoichiometric amounts of CaCO_3 and Nb_2O_5 . The powder mixture was heated at 1200 °C for 12 h in an alumina crucible. The obtained powder (1.00 g) was mixed with 1.0 mol L^{-1} HCl (100 mL), and the solution was changed daily for three days to produce the proton-exchanged product $\text{HCa}_2\text{Nb}_3\text{O}_{10} \cdot 0.5\text{H}_2\text{O}$.²⁹ Nanosheets of $\text{TBA}_{0.24}\text{H}_{0.76}\text{Ca}_2\text{Nb}_3\text{O}_{10}$ were obtained by mixing 0.12 g $\text{HCa}_2\text{Nb}_3\text{O}_{10} \cdot 0.5\text{H}_2\text{O}$ with 50 mL of 25.0 mmol L^{-1} tetra(n-butylammonium) hydroxide (TBA^+OH^-) solution and stirring overnight.²⁶

Na-TSM ($\text{Na}_{0.66}\text{Mg}_{2.68}(\text{Si}_{3.98}\text{Al}_{0.02})\text{O}_{10.02}\text{F}_{1.96}$) (1.00 g) was added to 100 mL deionized water and stirred overnight to exfoliate into nanosheets. Concentrated NaOH was used to bring the Na-TSM solution to a pH of 12.0 before metal oxide/hydroxide nanoparticle deposition. Commercially purchased SiO_2 with an average particle diameter of (17 ± 6) nm ($n = 101$) and a surface area of (408 ± 8) $\text{m}^2 \text{g}^{-1}$ was also brought to a pH of 12.0 before nanoparticle deposition.

Cobalt hydroxide, nickel hydroxide, copper oxide and silver oxide nanoparticles were deposited as previously reported for rhodium hydroxide nanoparticle deposition.^{26,30,31} 20 mmol L^{-1} aqueous solutions were made from the metal salts CoBr_2 , $\text{NiSO}_4 \cdot 6\text{H}_2\text{O}$, CuSO_4 , and AgNO_3 . Appropriate amounts of the metal aqueous solutions were added to 50.0 mL exfoliated nanosheets to achieve a metal mass fraction deposition of 0.05. The reaction was stirred for 18 h at room

temperature. The nanosheets were then restacked by dripping the suspension into 2 mol L^{-1} KOH (50 mL). The solid sample was washed twice more with KOH and three times with water before drying at 60 °C overnight.

An iridium colloidal solution containing both monomeric iridium ($[\text{Ir}(\text{OH})_5(\text{H}_2\text{O})]^{2-}$) and $\text{IrO}_x \cdot n\text{H}_2\text{O}$ nanoparticles was synthesized as previously reported.³² In the modified preparation, 2.0 mmol K_2IrCl_6 was dissolved in 80 mmol L^{-1} NaOH (90.0 mL), heated rapidly until the temperature reached 75 °C, then immediately cooled in an ice bath for 64 h. During the 64 h of ice bath cooling, the pH was monitored closely and kept at 11.9 with the addition of 1.0 mol L^{-1} NaOH. After 64 h, the solution volume was adjusted to 100 mL with nanopure water. Purified $\text{IrO}_x \cdot n\text{H}_2\text{O}$ nanoparticles were obtained by precipitating the above product with double volume isopropyl alcohol (IPA) and re-suspending the precipitate in deionized water.³² A more dilute 0.5 mmol L^{-1} iridium monomer solution (which contains little or no colloidal $\text{IrO}_x \cdot n\text{H}_2\text{O}$) was synthesized by the addition of 0.025 mmol K_2IrCl_6 to 50.0 mL of 0.100 mmol L^{-1} TBA^+OH^- , heating the solution to 70 °C until the solution turned colorless, and then being cooled immediately in an ice bath.³² The iridium species were deposited by adding 1.6 mL of the 20 mmol L^{-1} solution to 50.0 mL of the nanosheet solution to achieve a mass fraction of 0.05. The nanosheets were restacked as detailed above for the other nanoparticles.

For nanoparticles deposited onto Na-TSM, the composite was centrifuged without KOH restacking and washed three times with water before drying overnight at 60 °C.

Characterization. Isothermal titration calorimetry (ITC) experiments were performed using a 1.04 mL cell. Measurements were conducted as previously reported.²⁶ Aqueous metal halide precursors (10 mmol L^{-1} to 15 mmol L^{-1}) were injected from the syringe into solutions of $\text{TBA}_{0.24}\text{H}_{0.76}\text{Ca}_2\text{Nb}_3\text{O}_{10}$ nanosheets (0.1 mmol L^{-1} to 4 mmol L^{-1}). The iridium monomer solution was injected as a 0.5 mmol L^{-1} solution. A titration occurred every 25 min for the duration of the experiment (34 titrations). Experiments were done at 25 °C and in triplicate. The data was fit using an independent bonding model, and heats of dilution were subtracted from each run to retrieve thermochemical data.

High-resolution transmission electron microscopy (HRTEM) and high-angle annular dark field (HAADF) scanning transmission electron microscopy (STEM) images were obtained on a TEM with an accelerating voltage of 300 kV. For temperature-dependent TEM experiments, samples were dispersed in an IPA solution, drop cast on a temperature-controlled support and then dried under a heat lamp. Ambient temperature TEM images were retrieved after drop-casting sample from solution onto a lacey carbon TEM grid.

A powder X-ray diffractometer with monochromatized Cu $\text{K}\alpha$ radiation and a wavelength of 0.15418 nm was used to obtain powder X-ray diffraction (XRD) patterns.

For all measured values, the uncertainty is given as one standard deviation of the mean. The number of measurements for a measured value (n) is given throughout the text.

Electronic structure calculations. DFT calculations were conducted utilizing the Vienna *ab initio* simulation package (VASP).^{33,34} The exchange-correlation energy functional was treated using the generalized gradient approximation (GGA) implemented in the Perdew-Wang formulation (PW91).³⁵ Plane-wave basis sets were employed for all periodic calculations with an energy cut-off of 450 eV (4.34×10^4 kJ mol⁻¹). The projector augmented wave pseudo potential approximation³⁶ (PAW) was used to represent core electronic regions, with the following electronic valence configurations: 4p⁶4d⁴5s¹ for Nb, 3p²3d⁶4s² for Ca, 3s²3p² for Si, 2s²2p⁴ for O, 1s¹ for H, 3d⁷4s² for Co, 4p⁶4d⁸5s¹ for Rh, 5d⁷6s² for Ir, 3d⁸4s² for Ni, 4d¹⁰ for Pd, 5d⁹6s¹ for Pt, 3d¹⁰4s¹ for Cu, 4d¹⁰5s¹ for Ag, and 5d¹⁰6s¹ for Au. All calculations were spin polarized, and when necessary, multiple spin states were tested to ensure that the optimal spin state was identified. Monkhorst-Pack³⁷ (MP) Brillouin zone sampling was employed with a $4 \times 4 \times 1$ MP k-point spacing for calculations on the HCa₂Nb₃O₁₀ surface model (this was reduced to $3 \times 3 \times 1$ MP for the 2×2 supercell model used for calculations involving larger M₄ clusters), and a $2 \times 2 \times 1$ MP k-point sampling for the SiO₂ surface model. Single metal atom calculations were completed in a $4.5 \text{ nm} \times 4.5 \text{ nm} \times 4.5 \text{ nm}$ periodic box at the Γ point. Conjugant gradient structural relaxations were employed with an atomic force convergence criterion of 0.05 eV Å⁻¹ (48.2 kJ mol⁻¹ nm⁻¹). Partial charges on atoms were computed using the Bader method.^{38,39}

Results and Discussion

Nanoparticle deposition on layered oxide supports. Nanosheets derived from the layer perovskite KCa₂Nb₃O₁₀, and the synthetic mica Na-TSM were used as model early transition metal oxide and main group oxide supports, respectively. As in our earlier study,²⁶ the use of these nanosheets enabled observation of nanoparticle growth on the crystallographically well-defined basal plane surface, and provided thin, electron-transparent samples for imaging of the nanoparticles by HRTEM and HAADF-STEM. The phase purity of KCa₂Nb₃O₁₀ and its acid-exchanged derivative HCa₂Nb₃O₁₀·1.5 H₂O were confirmed by comparing XRD patterns to literature reports.²⁸ HCa₂Nb₃O₁₀·1.5 H₂O was exfoliated into nanosheets of TBA_{0.24}H_{0.76}Ca₂Nb₃O₁₀ in excess aqueous TBA⁺OH⁻ solutions as described previously.^{26,29}

Our earlier study quantified the heat of interfacial bonding between Rh³⁺ hydroxide nanoparticles and oxide supports. To more broadly investigate periodic trends, the oxides/hydroxides of five additional late transition metal ions (Ir³⁺, Co²⁺, Ni²⁺, Cu²⁺, Ag⁺) were investigated. These ions were selected based on the solubility of their halide salts and, in all cases except Ir³⁺, the rapid ligand exchange kinetics of the metal aquo ions. Metal oxide/hydroxide nanoparticles were deposited onto TBA_{0.24}H_{0.76}Ca₂Nb₃O₁₀ and Na-TSM nanosheets by *in situ* alkaline hydrolysis of the metal salt precursor, at a mass fraction of 0.05 metal. The same metal salts were used in ITC experiments to measure the interfacial bonding heats, as described below. Table S1 lists the metal precursors used in this study, as well as the corresponding metal oxide/hydroxide nanoparticles formed. The phase of the deposited nanoparticle was determined by hydrolyzing the precursor salts in TBA⁺OH⁻ in the absence of nanosheets, collecting the precipitate and identifying the solid by XRD (Figure S1).

The lattice constants of the nanoparticles made by hydrolysis in the absence of nanosheets are reported in Table S1. The XRD line widths indicate that Co(OH)₂ and CuO scattering domains are small, with estimated sizes of 5 nm and 13 nm, respectively. The linewidths predict the Ag₂O scattering domains to be larger, with an estimated size of 30 nm. The Ni(OH)₂ XRD pattern contains both narrow and broad reflections, consistent with the platy texture of this layered compound, with estimated scattering domain sizes of 12 nm and 2 nm, respectively.

Since Ir³⁺ complexes have slow ligand exchange rates, direct alkaline hydrolysis of Ir(III) halides was impractically slow for ITC experiments. In this case, pre-formed aquo ions and colloidal particles were made by alkaline hydrolysis and then deposited onto the nanosheets. We have recently shown that the dissolution of dilute Ir(III) and Ir(IV) salts in alkaline solutions (pH > 13, [Ir] < 10⁻⁴ mmol L⁻¹) produces monomeric anions ([Ir(OH)₅(H₂O)]²⁻ and [Ir(OH)₆]²⁻), and that condensation of these ions at higher concentrations yields amorphous IrO_x·nH₂O nanoparticles, onto which the monomeric anions strongly adsorb.^{32,40} This colloidal solution, with an average nanoparticle diameter of $(1.2 \pm 0.3) \text{ nm}$ ($n = 299$), is shown in the TEM image in Figure S2.

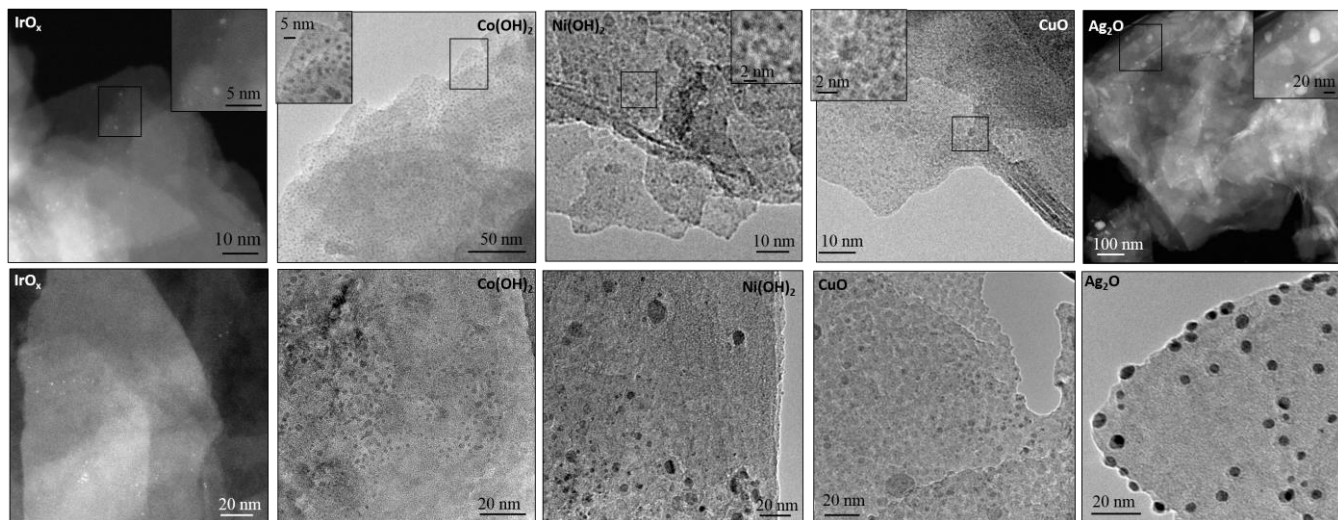


Figure 1. Ambient temperature HRTEM and HAADF STEM images of nanoparticles deposited at room temperature on $\text{KCa}_2\text{Nb}_3\text{O}_{10}$ (top) and Na-TSM (bottom).

This colloidal solution will be referred to as hydroxyiridate-capped $\text{IrO}_x \cdot n\text{H}_2\text{O}$ throughout this paper.

As we reported previously for $\text{Rh}(\text{OH})_3$ nanoparticle deposition on $\text{KCa}_2\text{Nb}_3\text{O}_{10}$, turbostratic restacking of the nanosheets occurs upon addition of KOH to the suspensions. The XRD patterns of the restacked materials show only 00 l and $hk0$ reflections of the nanosheets, and no reflections can be attributed to the nanoparticles.³⁰ All the late transition metal oxide/hydroxides deposited onto $\text{KCa}_2\text{Nb}_3\text{O}_{10}$ display these characteristic XRD patterns after restacking with KOH (Figure S3).

The HRTEM and HAADF STEM images on the top row of Figure 1 illustrate the size distribution of hydroxyiridate-capped $\text{IrO}_x \cdot n\text{H}_2\text{O}$, $\text{Co}(\text{OH})_2$, $\text{Ni}(\text{OH})_2$, CuO , and Ag_2O nanoparticles deposited onto $\text{TBA}_{0.24}\text{H}_{0.76}\text{Ca}_2\text{Nb}_3\text{O}_{10}$ nanosheets at ambient temperature, and Table 1 lists the deposited nanoparticle average diameter. Except in the case of Ag_2O , there is a spatially uniform distribution of nanoparticles on the niobate support. The average diameter of the Ag_2O particles (7 nm) is much larger than the other deposited nanoparticles (1 nm–2 nm).

For comparison purposes, the same nanoparticles were deposited onto the layered silicate Na-TSM. Na-TSM contains tetrahedral-octahedral-tetrahedral (T-O-T) silicate layers separated by Na^+ ions (Figure S4). Each tetrahedral layer is capped by oxygen atoms shared by two T atoms, and therefore there are no free Si-OH groups on the basal plane surface. The saturation loading of nanoparticles and their distribution onto Na-TSM was in stark contrast to nanoparticles deposited onto $\text{KCa}_2\text{Nb}_3\text{O}_{10}$, as shown in the bottom row of images in Figure 1. There was a broader size distribution of nanoparticles, as well as areas of the support with no nanoparticles present, and there were also large particles in the suspension, as seen in the TEM, that were not bound to the support in the case of both CuO and Ag_2O .

Table 1. Average nanoparticle diameter of metal oxide/hydroxide nanoparticles deposited onto nanosheets of $\text{TBA}_{0.24}\text{H}_{0.76}\text{Ca}_2\text{Nb}_3\text{O}_{10}$ and Na-TSM at room temperature as determined from TEM analysis. The number in parentheses represents the number of measurements used to determine one standard deviation of the mean.

	$\text{TBA}_{0.24}\text{H}_{0.76}\text{Ca}_2\text{Nb}_3\text{O}_{10}$	Na-TSM
Metal NP	Diameter (nm) (<i>n</i>)	Diameter (nm) (<i>n</i>)
$\text{IrO}_x \cdot n\text{H}_2\text{O}$	0.9 ± 0.2 (151)	1.3 ± 0.5 (53)
$\text{Co}(\text{OH})_2$	1.2 ± 0.5 (304)	2.1 ± 0.5 (154)
$\text{Ni}(\text{OH})_2$	1.3 ± 0.4 (153)	6 ± 3 (201)
CuO	2.0 ± 0.6 (320)	6 ± 5 (66)
Ag_2O	7 ± 5 (216)	5 ± 2 (219)

In our earlier study, micron-sized $\text{Rh}(\text{OH})_3$ particles were found to break up and deposit as < 1 nm diameter particles on nanosheets of $\text{TBA}_{0.24}\text{H}_{0.76}\text{Ca}_2\text{Nb}_3\text{O}_{10}$.²⁶ This “reverse” ripening effect was attributed to the thermodynamically favorable interaction between $\text{Rh}(\text{OH})_3$ and the oxide support, which overcomes the surface energy penalty of forming smaller particles. “Reverse” ripening experiments were performed on Co, Ni, Cu, and Ag oxide/hydroxide particles by hydrolyzing the metal halide precursors in TBA^+OH^- for 18 h before their addition to a suspension of $\text{TBA}_{0.24}\text{H}_{0.76}\text{Ca}_2\text{Nb}_3\text{O}_{10}$ nanosheets in 25 mmol L^{-1} TBA^+OH^- .

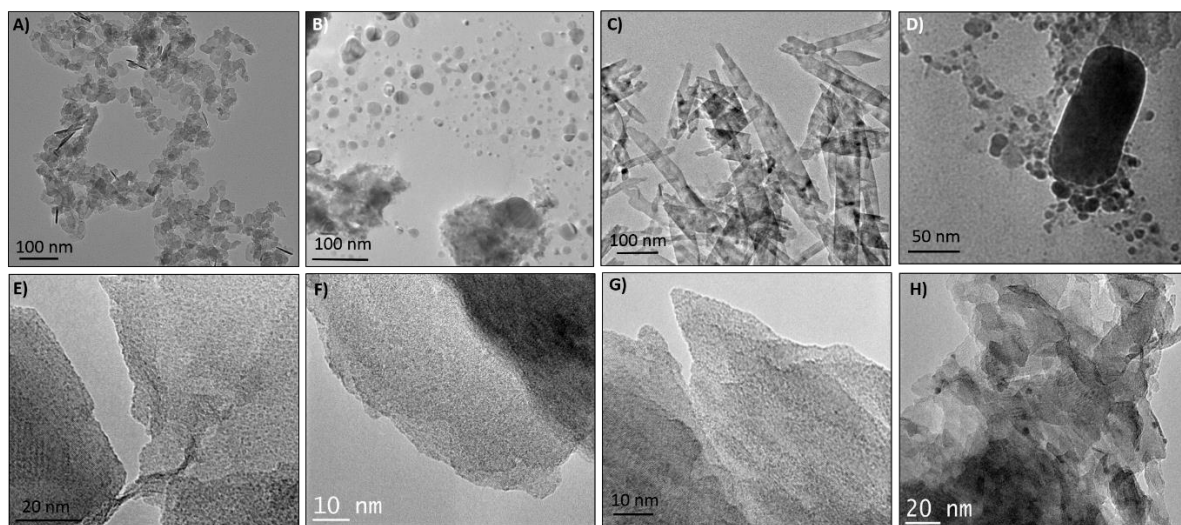


Figure 2. TEM images from “reverse” ripening experiments in which pre-formed particles were mixed with suspensions of $\text{TBA}_{0.24}\text{H}_{0.76}\text{Ca}_2\text{Nb}_3\text{O}_{10}$ nanosheets. Panels A – D show pre-formed particles of $\text{Co}(\text{OH})_2$, $\text{Ni}(\text{OH})_2$, CuO and Ag_2O , respectively. E – H show the nanoparticles derived from the same elements, respectively, after deposition onto the nanosheets.

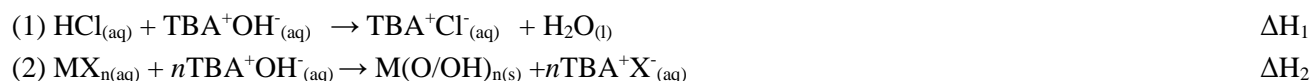
In all cases, the deposited nanoparticles were smaller after addition of the nanosheet suspension, and in a few cases, the shape of the nanoparticles changed dramatically. For example, CuO particles formed in the absence of nanosheets were rods with an outer diameter of (19 ± 13) nm ($n = 95$), $\text{Co}(\text{OH})_2$ particles were both thin platelets with an average lateral dimension of (22 ± 11) nm ($n = 193$) and rods, and $\text{Ni}(\text{OH})_2$ particles were a mixture of spherical particles, platelets and wires (not all shapes are pictured in Figure 2b). Upon addition of the pre-formed metal oxide/hydroxide particles to colloidal $\text{TBA}_{0.24}\text{H}_{0.76}\text{Ca}_2\text{Nb}_3\text{O}_{10}$, all the metal oxides/hydroxides deposited as much smaller nanoparticles and no rod-shaped particles were found. Not all of the pre-formed $\text{Co}(\text{OH})_2$ and Ag_2O particles deposited on the nanosheets, and $\text{Co}(\text{OH})_2$ particles deposited with a broad size distribution on different areas of the nanosheets. Figure 2 shows TEM images of the pre-formed nanoparticles (top) and their deposition onto $\text{TBA}_{0.24}\text{H}_{0.76}\text{Ca}_2\text{Nb}_3\text{O}_{10}$ nanosheets (bottom).

ITC measurements of interfacial bonding energies. The interaction heats between metal oxide/hydroxide nanoparticles and oxide supports were measured by using ITC titrations as previously described.²⁶ The deposition of the nanoparticles onto an oxide support involves several chemical steps, and therefore, the enthalpy change that corresponds to the nanoparticle-support interaction must be obtained by difference from the overall heat of reaction.

Scheme 1 shows a generic Born-Haber cycle for the deposition of a metal oxide/hydroxide ($\text{M}(\text{O}/\text{OH})_{(s)}$) from a metal halide precursor ($\text{MX}_{(aq)}$). The overall enthalpy change of the reaction (ΔH_4) is the sum of the enthalpies of bonding (ΔH_3),

hydrolysis (ΔH_2), and neutralization (ΔH_1). This Born-Haber cycle was used for cobalt, nickel, copper and silver deposition. The enthalpy of neutralization ($\Delta H_1 = (-58 \pm 2)$ kJ mol⁻¹) was included only in cases when hydrolysis of the metal salt precursor generated acid. The deposition of iridium oxide represents a special case, since we have recently found that colloidal solutions of ligand-free $\text{IrO}_x \cdot n\text{H}_2\text{O}$ nanoparticles prepared by alkaline hydrolysis of $[\text{IrCl}_6]^{2-}$ solutions contain strongly adsorbed hydroxyiridate ions $[\text{Ir}(\text{OH})_5(\text{H}_2\text{O})]^{2-}$ and $[\text{Ir}(\text{OH})_6]^{2-}$.³² ITC experiments were performed to measure the heats of adsorption of each individual component. First, the $\text{IrO}_x \cdot n\text{H}_2\text{O}$ colloidal solution was purified as previously reported to remove the monomeric anions from the surface of the nanoparticles.³² Interestingly, there was no measurable heat of interaction between these purified particles and $\text{TBA}_{0.24}\text{H}_{0.76}\text{Ca}_2\text{Nb}_3\text{O}_{10}$ nanosheets. Next, the heat of interaction between the monomeric anions and nanosheets was measured and found to be -83 ± 17 kJ mol⁻¹. From these data, it could be concluded that only the monomeric anions are interacting with the support when $\text{IrO}_x \cdot n\text{H}_2\text{O}$ nanoparticles are deposited onto the nanosheets. Therefore, we use the interaction heat of the monomeric anions in plotting the periodic trends below (Figure 3). It should be noted that alkaline solutions of the monomer in equilibrium with air contain both Ir^{III} and Ir^{IV} forms of the monomer ($[\text{Ir}(\text{OH})_5(\text{H}_2\text{O})]^{2-}$ and $[\text{Ir}(\text{OH})_6]^{2-}$, respectively), but EPR experiments show that the predominant form is Ir^{III} ,³² and therefore we refer to the equilibrium mixture of anions simply as $[\text{Ir}(\text{OH})_5(\text{H}_2\text{O})]^{2-}$.

Scheme 1. General Born-Haber cycle for metal oxide/hydroxide nanoparticle deposition onto oxide supports during ITC experiments.



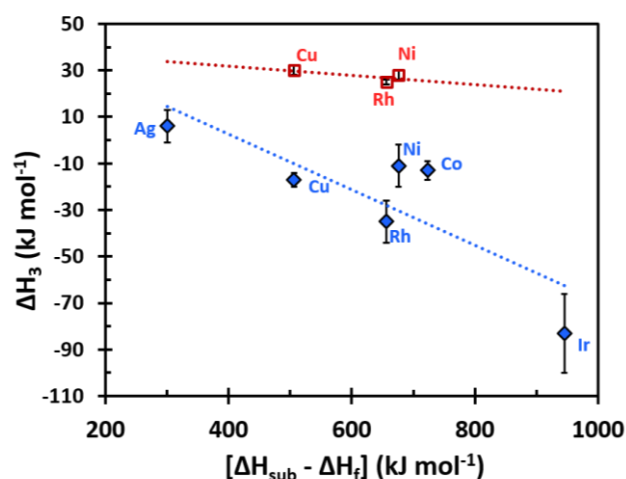
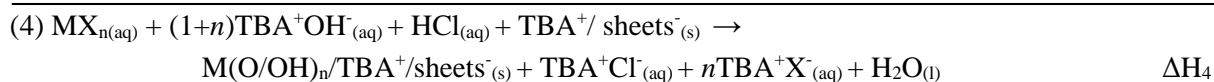


Figure 3. Thermochemical data for heats of interaction between metal oxide/hydroxide nanoparticles (or monomeric anions in the case of Ir) and supports for $\text{TBA}_{0.24}\text{H}_{0.76}\text{Ca}_2\text{Nb}_3\text{O}_{10}$ nanosheets (blue diamonds) and high surface area silica (red squares). The SiO_2 nanoparticle support had an average particle diameter of (17 ± 6) nm ($n = 101$) and a surface area of (408 ± 8) $\text{m}^2 \text{g}^{-1}$. Enthalpy changes are plotted per mole of transition metal M. The x-axis represents M-O bond strength as the difference between the heat of sublimation of the bulk metal and the heat of formation of its most stable oxide.

Figure 3 shows the molar enthalpy of adsorption of the metal nanoparticles (or monomer in the case of Ir^{III}) to $\text{TBA}_{0.24}\text{H}_{0.76}\text{Ca}_2\text{Nb}_3\text{O}_{10}$ nanosheets, plotted against $[\Delta H_{\text{sub}} - \Delta H_f]$, the difference between the sublimation enthalpy of the bulk metal and the heat of formation of the most stable metal oxide (experimental values of ΔH_{sub} and ΔH_f used for each metal are provided in Table S2). This quantity represents the heat of forming the metal oxide from metal atoms and thus follows the trend in M-O bond energy. These enthalpy changes are plotted as kJ per mole of metal atoms. The ΔH_3 values span a broad range, from quite exothermic to mildly endothermic. The strongest bonding to the niobate sheets is $[\text{Ir}(\text{OH})_5(\text{H}_2\text{O})]^{2-}$ with an interaction heat of (-83 ± 17) kJ mol^{-1} , while the weakest is with Ag_2O at (6 ± 7) kJ mol^{-1} . This endothermic heat of interaction can be measured since the enthalpy of the overall reaction is favorable; that is, reactions 1 and 2 drive the adsorption of nanoparticles to the support. The general trend is toward weaker interfacial bonding as the strength of the M-O bond in the bulk oxide decreases, as observed in earlier calorimetric studies of metal clusters binding to oxide

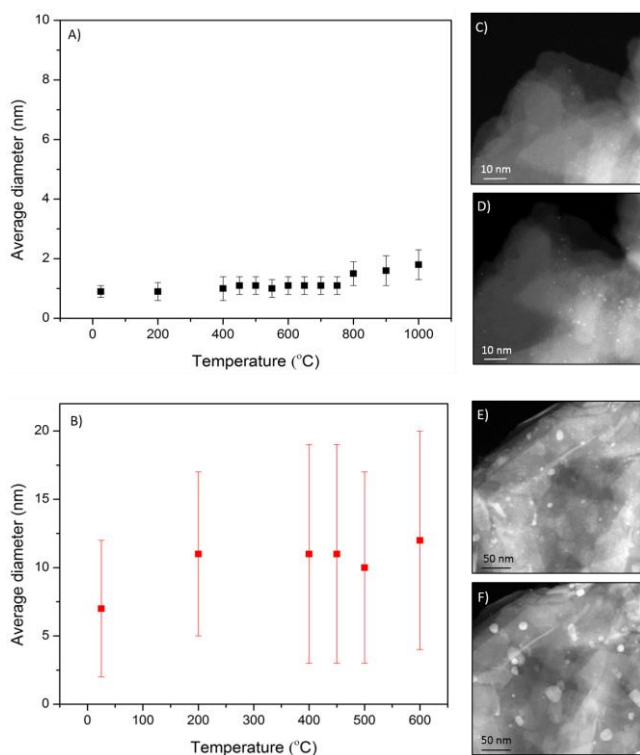


Figure 4. Plots of the average particle diameter of A) hydroxyiridate-capped $\text{IrO}_x \cdot n\text{H}_2\text{O}$ and B) Ag_2O deposited on $\text{TBA}_{0.24}\text{H}_{0.76}\text{Ca}_2\text{Nb}_3\text{O}_{10}$ nanosheets, after restacking with KOH. The uncertainty in each measurement is reported as one standard deviation of the mean for n measurements. (Supporting information, Table S3). HAADF STEM images of hydroxyiridate-capped $\text{IrO}_x \cdot n\text{H}_2\text{O}$ supported on $\text{KCa}_2\text{Nb}_3\text{O}_{10}$ at C) 25 °C and D) 700 °C. E) and F) are HAADF STEM images of Ag_2O on $\text{KCa}_2\text{Nb}_3\text{O}_{10}$ at 25 °C and 700 °C, respectively.

supports,⁵ although this is the first demonstration of this correlation for binding from a liquid-phase metal precursor solution. While the same trend is followed for metals on the silica support, in that case, the interaction energies are endothermic and there is less of a difference between elements with stronger and weaker M-O bonding.

It is apparent from the comparison of Table 1 and Figures 2 and 3 that well-dispersed and smaller nanoparticles are grown on the niobate support as the heat of interaction becomes more exothermic. Upon deposition, $\text{Rh}(\text{OH})_3$ nanoparticles on $\text{TBA}_{0.24}\text{H}_{0.76}\text{Ca}_2\text{Nb}_3\text{O}_{10}$ have an average diameter of less than 1 nm and a heat of interaction of (-35 ± 9) kJ mol^{-1} .²⁶ In contrast Ag_2O has a slightly endothermic interaction heat (6 ± 7) kJ mol^{-1} and deposits at room temperature as unevenly distributed particles with an average size diameter of (7 ± 5) nm. The broad distribution of particle sizes for the metal oxides studied on Na-TSM (Table 1) correlates with the endothermic interaction energy with the high surface area silica support. The resistance of supported nanoparticles to sintering (see Supporting Information) follows a similar trend in which the thermodynamic driving force for

particle growth is reduced by a strong bonding interaction of the nanoparticle with the support. Therefore, hydroxyiridate-capped $\text{IrO}_x \cdot n\text{H}_2\text{O}$ nanoparticles deposited on a niobium support are remarkably resistant to sintering at temperatures up to 1000 °C.

Computational modeling of particle-support interactions. Campbell and co-workers have shown that metals that bond more strongly to oxygen also interact more exothermically with oxide supports.⁵ In their experiments, like those described here, the composition of the support has a clear effect on the strength of this interaction.⁵ “Strong” supports such as CeO_2 and Fe_3O_4 are differentiated from “weak” supports such as MgO by their more exothermic bonding to noble metal nanoparticles.^{4,5} To better understand the nature of the interfacial interaction, the first set of DFT electronic structure calculations done in this work used a range of metals (Au, Ag, Cu, Pt, Pd, Ni, Ir, Rh, and Co) and models for representative oxide supports ($\text{HfCa}_2\text{Nb}_3\text{O}_{10}$ and SiO_2). Because the extent of nanoparticle reduction in the experimental particle growth studies is unknown, and since previous experiments show similar trends for growth of $\text{Rh}(\text{OH})_3$ nanoparticles when heated in vacuum and reducing atmospheres, we initially used fully reduced metal atoms and clusters to simplify the modeling. The calculations were then extended to metal atoms and clusters in higher oxidation states, which qualitatively show the same trends in bonding strength (see below).

The calcium niobate nanosheets were modeled in their proton-exchanged form ($\text{HfCa}_2\text{Nb}_3\text{O}_{10}$) by first optimizing the bulk structure, beginning with the experimentally characterized P4/*mbm* crystal structure refined by Chen *et al.*²⁹ The DFT-optimized bulk lattice constants were $a = b = 0.534$ nm and $c = 1.464$ nm, in reasonable agreement with the experimental values of $a = b = 0.545$ nm and $c = 1.441$ nm. From the optimized computed structure, the surface of the layered oxide was cleaved in the [001] direction, which is the layering axis of the crystal. H_2O molecules that occupy the inter-layer galleries in the bulk structure were not included in the computational model. The resulting surface structure of the $\text{HfCa}_2\text{Nb}_3\text{O}_{10}$ support is shown in Figure S7.

The SiO_2 support was modeled using a reconstructed, partially hydroxylated β -cristobalite $\text{SiO}_2(001)$ surface structure reported by Rozanska *et al.*, which is predicted to be stable under the conditions employed in this study and is commonly used to model amorphous silica supports.⁴¹

Binding energies for both single metal atoms and four-atom tetrahedral clusters (denoted M_4) were calculated to model metal-oxide support interaction strengths. Binding energies were calculated relative to the clean oxide surface plus a gas phase metal atom (or cluster): $E_{\text{bind}} = E_{\text{metal/support}} - E_{\text{support-clean}} - E_{\text{metal-[g]}}$, where $E_{\text{metal-[g]}}$ is the energy of the gas phase metal atom (or cluster), $E_{\text{support-clean}}$ is the energy of the clean support surface, and $E_{\text{metal/support}}$ is the energy of the metal-adsorbed surface. Negative values indicate exothermic binding.

For single atoms, structural optimization calculations were initiated from three possible surface binding sites on the $\text{HfCa}_2\text{Nb}_3\text{O}_{10}$ surface: (1) the equatorial oxygen, (2) the axial oxygen, or (3) the interstitial space between NbO_6 polyhedra

(Figure S7A). The optimized structure of Ir and Ag atoms are shown in Figure 5A and 5B, respectively, and demonstrate that the equatorial oxygen site is preferred for Ir, which interacts strongly, whereas the interstitial site is preferred for Ag, which interacts more weakly. In both cases, there is a resulting close contact between the adsorbed metal and niobium atoms in the support. For Ir and Ag, the optimized metal-niobium distances are 0.27 nm and 0.31 nm, respectively. This suggests that metal-metal bonding between the adsorbed metal and the underlying niobium atom is indeed possible. The optimized structure of all the metal atoms studied on $\text{HfCa}_2\text{Nb}_3\text{O}_{10}$ are shown in Figure S8, where similar metal-metal distances (Table S4) were observed, except for Au, which preferred the axial oxygen binding site. The optimized single atom metal adsorption site for SiO_2 binding is the same for all metals and is represented in Figure S9.

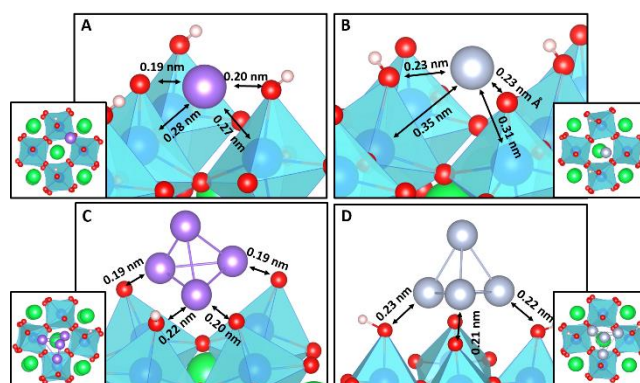


Figure 5. Optimized adsorption geometries on $\text{HfCa}_2\text{Nb}_3\text{O}_{10}$ for single atoms of (A) Ir and (B) Ag and M_4 clusters of (C) Ir and (D) Ag.

The optimized M_4 adsorption structures for Ir and Ag on $\text{HfCa}_2\text{Nb}_3\text{O}_{10}$ are provided in Figure 5C and 5D, respectively. Both of these metallic clusters prefer the interstitial bonding site with a 3-atom basal plane in contact with surface oxygen atoms, although Ag_4 sits flat above the surface. The optimized M_4 adsorption structures for all the metals, shown in Figure S10, demonstrate that all metals (except Au) prefer the interstitial site with the 3-atom basal plane in contact with the surface. The bond distances are shown in Table S5.

In Figure 6A-B, the resulting binding energies are plotted against $[\Delta H_{\text{sub}} - \Delta H_f]$ for each metal. A linear correlation between the oxide formation energy and the metal-support binding strength emerges from the calculations. The niobate and silicate supports are strong and weak, respectively, as also shown in the experimental data in Figure 3.

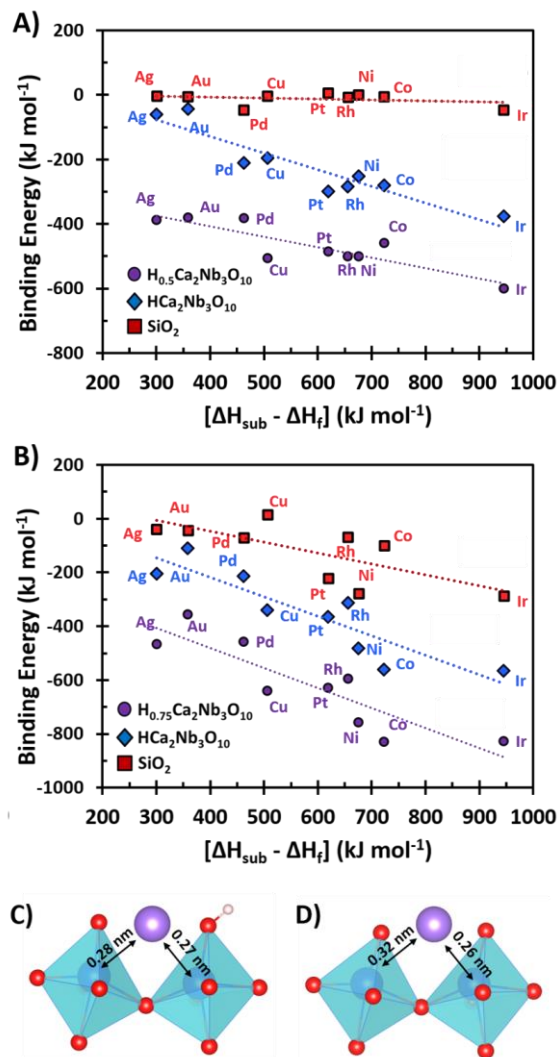


Figure 6. Binding energies for (A) single metal atoms and (B) M₄ metal clusters on niobium oxide and silica surfaces plotted against the formation enthalpy of the corresponding metal's most stable oxide calculated relative to a single gas phase metal atom, $[\Delta H_{\text{sub}} - \Delta H_f]$. Structural interfaces of iridium adsorbed to (C) stoichiometric and (D) non-stoichiometric niobium oxide surfaces.

This type of correlation was first proposed and experimentally demonstrated by Campbell and Sellers⁵ and can serve as a useful computational screening tool for selecting candidates for supported catalytic metals with specific interaction strengths. The plots in Figure 6 demonstrate that platinum-group metals bind strongly to the niobate support, whereas late transition metals interact weakly with the silica support. The resulting periodic trend in interaction strength across late transition metal atoms and clusters is in agreement with the experimental trend in adsorption strengths of metal oxides (ΔH_3) determined by ITC and shown in Figure 3. The DFT calculations are also consistent with the experimental observation that the composition of the support strongly affects the interfacial bonding enthalpy. All metal nanoparticles investigated interact weakly with the SiO₂ support, as shown experimentally in Figure 3 and computationally in Figure 6.

The effect of the oxidation state of the metal atom was then investigated for comparison with the experimentally measured heats of interaction determined by ITC. The binding energies of all metals were calculated on an H_{0.5}Ca₂Nb₃O₁₀ surface model, which changed the formal oxidation state of the metal from M⁰ to M¹⁺. This yields an oxidation state equivalent to adsorbing a metal atom with an attached -OH group (and desorbing H₂O in the adsorption process). The data in Figure 6A show stronger adsorption to the H_{0.5}Ca₂Nb₃O₁₀ surface than to the stoichiometric surface, and the same qualitative trend in bonding strength is obtained regardless of the oxidation state of the metal. Figure 6C-D compares the structural interface models of iridium calculated in different oxidation states. The Ir-Nb bond distance is decreased over the H_{0.5}Ca₂Nb₃O₁₀ surface, reflecting stronger binding induced by the Ir-Nb interaction. The good correlation between theory and experiment suggests that the periodic trends in nanoparticle/support interactions are insensitive to the metal oxidation state, as observed experimentally in the Rh/Rh(OH)₃ case.²⁶ This suggests that DFT modeling can be used to investigate a broader range of metals than might be experimentally accessible for ITC thermodynamic analysis.

Analysis of metal-support electronic structures provides insight into the nature of the metal-oxide support bonding. The difference in bonding character between Ir and Ag on the niobium oxide is demonstrated by the density of states (DOS) analysis shown in Figure 7. In Figure 7A, there is clear mixing of Ir and Nb d-states, indicative of electron transfer from Ir atoms to the nearest adjacent niobium atoms in the support. This suggests some degree of metal-metal bonding and is further confirmed by the Bader charge differences (calculated as the Bader charge of the surface-bound metal atom relative to the valence of the gas phase metal atom) reported in Table S6. A pronounced negative charge depletion on the surface-bound Ir atom is observed. The isostructural plots in Figure 7 show the charge density difference calculated between the full metal-support system and the clean-support/metal-atom components, revealing how charge is transferred between the cluster and the support. For the iridium cluster, there is significant valence electron density between Ir and Nb at the interface demonstrated by the purple isosurface, which again suggest a strong Ir-Nb bonding interaction. Conversely, no mixing of d-states between Ag and niobium is seen in the DOS plots in Figure 7B, resulting in a high energy gap state relative to the d-band and weak Ag binding. Correspondingly, there is no valence electron density accumulation between the cluster and support in the Ag system seen in the charge density difference. This conclusion is also consistent for the bonding between the niobium support and single metal atoms, as shown in Figures S11 and S12, demonstrating that the results are not dependent on the chosen cluster model.

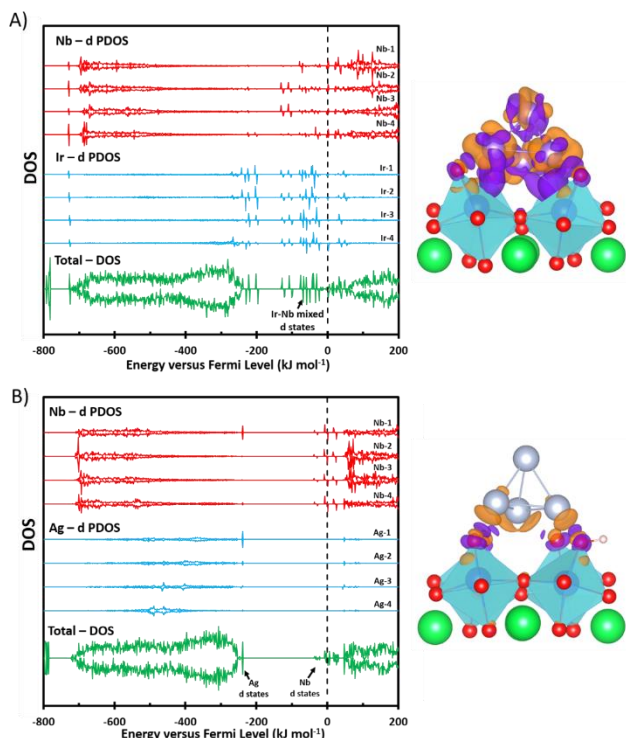


Figure 7. Total and partial density of states plotted relative to the Fermi level for $\text{HCa}_2\text{Nb}_3\text{O}_{10}$ supported (A) Ir and (B) Ag 4-atom clusters. The total DOS is shown in green, the PDOS projected on the d-states of the Nb surface atom adjacent to the adsorbed metal atom is shown in red, and PDOS projected on the d-states of the adsorbed metal atom is shown in blue. Spin up and spin down states are plotted on the positive and negative axes, respectively. The Fermi level is denoted by the vertical dotted line. Charge density difference isosurfaces are shown on the right, where the purple regions reflect negative charge accumulation and the orange regions reflect charge depletion. The accumulation and depletion isosurfaces are shown at values of $\pm 0.4 e \text{ nm}^{-1}$.

The Bader charge analysis for $\text{HCa}_2\text{Nb}_3\text{O}_{10}$ in Table S6 demonstrates that for all metals tested there is significant *negative charge transfer* from the transition metal atom to the niobate support, whereas there is little charge transfer to or from the transition metal to SiO_2 . In fact, for Ir and Ni on SiO_2 , there is actually a small amount of charge transfer *from* the support to the adsorbed metal; this is also reflected in the charge density difference plot for Ir- SiO_2 shown in Figure S13.

The role of d-orbital mixing in stabilizing bimetallic transition metal alloys and interfaces has a long history in the experimental and theoretical literature. Brewer proposed in 1967 that d-acid/base interactions between early and late transition metals, respectively, could account for the anomalous stability of alloys such as ZrPt_3 .⁴² Later electronic structure calculations by Wang and Carter, however, showed that in these alloys charge transfer occurred in the opposite direction, from the early to the late transition metal.⁴³ Strong evidence for electron transfer in the Brewer sense (from the more to the less electronegative metal) has been found for ultrathin films of late transition metals such as Pd, Ni, and Cu on earlier transition metal (Mo, W, Ru) surfaces.⁴⁴⁻⁴⁷ In these studies, Goodman concluded that the electronegativity of the surface atoms was lower than those in the bulk

metal.⁴⁵ The present results suggests that the Brewer d-acid/base interaction is quite relevant to the interaction of transition metal and metal oxide nanoparticles with “strong” supports, which have empty or partially filled d-orbitals. A key factor appears to be the coincidence of d-orbital energies in the relevant oxidation states of the two metals, as shown for Ir^0 and Nb^{5+} in Fig. 7A. It is interesting to note that Ag binds weakly to the niobate support because the d-orbitals of Ag are significantly lower in energy than those of Nb^{5+} . As demonstrated in Figures 3 and 6, metals that form stronger M-O bonds are also observed to bind stronger to the oxide support. Our electronic structure analysis, however, suggests that electron donation from the adsorbed metal atom occurs mainly to the Nb on the layered niobate structures, suggesting that the supported metal atoms oxidation tendencies can be predictive of strong support interactions independent from the destination of charge transferred upon adsorption. This suggests the possibility of tuning the strength of the metal-support interactions for late transition metals through appropriate choice of d-electron accepting oxide supports. Experiments along these lines are currently underway

Conclusions

Metal oxide and hydroxide nanoparticles ($\text{M} = \text{Co}, \text{Ni}, \text{Cu}, \text{Ag}$) and monomeric $[\text{Ir}(\text{OH})_5(\text{H}_2\text{O})]^{2-}$ anions were deposited onto niobium oxide and silicon oxide supports by alkaline hydrolysis of water-soluble metal salts. ITC and TEM data show a strong correlation between interfacial bonding strength and the inhibition of thermal sintering of the supported nanoparticles. These results are consistent with our earlier observations of $\text{Rh}(\text{OH})_3$ nanoparticles on early transition metal oxide and main group oxide supports.²⁶ Nanoparticles that bond exothermically to the oxide support, such as hydroxyiridate-capped $\text{IrO}_x \cdot n\text{H}_2\text{O}$ on $\text{KCa}_2\text{Nb}_3\text{O}_{10}$, deposit as $< 1 \text{ nm}$ particles and resist sintering even up to temperatures of 1000°C . In contrast, nanoparticles that interact endothermically with silica supports have a broad original size distribution and appear to migrate and coalesce rapidly at lower temperatures.

ITC data show that $\text{Ni}(\text{OH})_2$, CuO and $\text{Rh}(\text{OH})_3$ all interact endothermically with SiO_2 and exothermically with $\text{TBA}_{0.24}\text{H}_{0.76}\text{Ca}_2\text{Nb}_3\text{O}_{10}$ nanosheets. This trend is supported by DFT calculations, which also provide insight into the nature of the metal-support interaction. The strong interaction between late transition metal/metal oxide nanoparticles and the early transition metal oxide support $\text{HCa}_2\text{Nb}_3\text{O}_{10}$ can be attributed to the formation of mixed d-states and charge transfer from the supported metal atoms to the niobium atoms in the oxide support. These interactions are absent in weakly binding metals and a silicon oxide support. A strong correlation between the experimental measurements and theoretical calculations emerged in this work to confirm that the qualitative trends in metal bonding interaction are independent of the formal oxidation state of the supported metal. Together, these combined experimental and computational studies reveal the important role of d-orbital interactions in controlling the metal-support interaction, and underscore the importance of understanding how the support composition impacts nanoparticle bonding strength and stability.

ASSOCIATED CONTENT

Supporting Information. Details of obtaining thermochemical data from ITC experiments, XRD of bulk nanoparticles and nanoparticle/support composites, TEM and UV-Vis of hydroxyiridate-capped $\text{IrO}_x \cdot n\text{H}_2\text{O}$ particles, sintering studies of supported metal oxide nanoparticles, surface models used for DFT binding energy calculations, optimized single atom and metal cluster adsorption geometries, charge density difference plots, list of nanoparticles and metal precursors, and heats of formation of oxides and sublimation of metals (16 pp). This material is available free of charge via the Internet at <http://pubs.acs.org>.

DISCLAIMER

Certain commercial equipment, instruments, or materials (or suppliers, or software, ...) are identified in this paper to foster understanding. Such identification does not imply recommendation or endorsement by the National Institute of Standards and Technology, nor does it imply that the materials or equipment identified are necessarily the best available for the purpose.

AUTHOR INFORMATION

Corresponding Author

* tem5@psu.edu, mjanik@engr.psu.edu

ACKNOWLEDGMENT

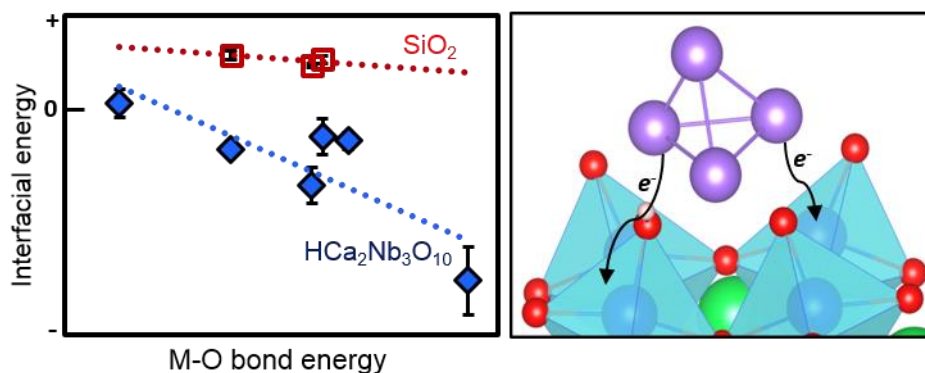
We thank Nicholas McCool for assistance with obtaining ambient temperature TEM images and helpful discussions, and Nicholas Sturgis for helpful ITC discussions. This work was supported by the National Science Foundation under grant DMR-1306938. MES and NMVB acknowledge National Science Foundation Graduate Fellowship grant DGE-1255832. TPS and MJJ acknowledge support from National Science Foundation grant CBET-1032979. RMR acknowledges funding from the Department of Energy, Office of Basic Energy Sciences, Chemical Sciences, Geosciences and Biosciences Division, Catalysis Sciences Program, under grant number DE-FG02-12ER16364. Additionally, RMR acknowledges funding from the Pennsylvania State University College of Engineering Instrumentation Grant Program for the purchase of a TA Instruments NanoITC.

REFERENCES

- (1) Goodman, D. W. *Chem. Rev.* **1995**, *95*, 523.
- (2) Haruta, M. *Catal. Today* **1997**, *36*, 153.
- (3) Shekhar, M.; Wang, J.; Lee, W.-S.; Williams, W. D.; Kim, S. M.; Stach, E. A.; Miller, J. T.; Delgass, W. N.; Ribeiro, F. H. *J. Am. Chem. Soc.* **2012**, *134*, 4700.
- (4) Campbell, C. T. *Acc. Chem. Res.* **2013**, *46*, 1712.
- (5) Campbell, C. T.; Sellers, J. R. V. *Faraday Discuss.* **2013**, *162*, 9.
- (6) Cargnello, M.; Doan-Nguyen, V. V. T.; Gordon, T. R.; Diaz, R. E.; Stach, E. A.; Gorte, R. J.; Fornasiero, P.; Murray, C. B. *Science* **2013**, *341*, 771.
- (7) Valden, M.; Lai, X.; Goodman, D. W. *Science* **1998**, *281*, 1647.
- (8) Vayssilov, G. N.; Lykhach, Y.; Migani, A.; Staudt, T.; Petrova, G. P.; Tsud, N.; Skála, T.; Bruix, A.; Illas, F.; Prince, K. C.; Matolín, V.; Neyman, K. M.; Libuda, J. *Nat Mater* **2011**, *10*, 310.
- (9) Mostafa, S.; Behafarid, F.; Croy, J. R.; Ono, L. K.; Li, L.; Yang, J. C.; Frenkel, A. I.; Cuenya, B. R. *J. Am. Chem. Soc.* **2010**, *132*, 15714.
- (10) Haruta, M. *CATTECH* **2002**, *6*, 102.
- (11) Bonanni, S.; Aït-Mansour, K.; Harbich, W.; Brune, H. *J. Am. Chem. Soc.* **2012**, *134*, 3445.
- (12) Hu, Z.; Nakamura, H.; Kunimori, K.; Asano, H.; Uchijima, T. *J. Catal.* **1988**, *112*, 478.
- (13) Tauster, S. J. *Acc. Chem. Res.* **1987**, *20*, 389.
- (14) Tauster, S. J.; Fung, S. C.; Baker, R. T. K.; Horsley, J. A. *Science* **1981**, *211*, 1121.
- (15) Wang, Y.-G.; Yoon, Y.; Glezakou, V.-A.; Li, J.; Rousseau, R. *J. Am. Chem. Soc.* **2013**, *135*, 10673.
- (16) Meyer, R.; Ge, Q.; Lockemeyer, J.; Yeates, R.; Lemanski, M.; Reinalda, D.; Neurock, M. *Surface Science* **2007**, *601*, 134.
- (17) Addou, R.; Senftle, T. P.; O'Connor, N.; Janik, M. J.; van Duin, A. C. T.; Batzill, M. *ACS Nano* **2014**, *8*, 6321.
- (18) Negreiros, F. R.; Fabris, S. *The Journal of Physical Chemistry C* **2014**, *118*, 21014.
- (19) Vilhelmsen, L. B.; Hammer, B. *Physical Review Letters* **2012**, *108*, 126101.
- (20) Bruix, A.; Lykhach, Y.; Matolínová, I.; Neitzel, A.; Skála, T.; Tsud, N.; Vorokhta, M.; Stetsovych, V.; Ševčíková, K.; Mysliveček, J.; Fiala, R.; Václavů, M.; Prince, K. C.; Bruyère, S.; Potin, V.; Illas, F.; Matolín, V.; Libuda, J.; Neyman, K. M. *Angewandte Chemie International Edition* **2014**, *53*, 10525.
- (21) Hansen, T. W.; DeLaRiva, A. T.; Challa, S. R.; Datye, A. K. *Accounts of Chemical Research* **2013**, *46*, 1720.
- (22) Fu, Q.; Yang, F.; Bao, X. *Acc. Chem. Res.* **2013**, *46*, 1692.

- (23) Hansen, P. L.; Wagner, J. B.; Helveg, S.; Rostrup-Nielsen, J. R.; Clausen, B. S.; Topsøe, H. *Science* **2002**, *295*, 2053.
- (24) Campbell, C. T.; Parker, S. C.; Starr, D. E. *Science* **2002**, *298*, 811.
- (25) Prieto, G.; Zečević, J.; Friedrich, H.; de Jong, K. P.; de Jongh, P. E. *Nat Mater* **2013**, *12*, 34.
- (26) Strayer, M. E.; Binz, J. M.; Tanase, M.; Kamali Shahri, S. M.; Sharma, R.; Rioux, R. M.; Mallouk, T. E. *J. Am. Chem. Soc.* **2014**, *136*, 5687.
- (27) Stuckless, J. T.; Frei, N. A.; Campbell, C. T. *Rev. Sci. Instrum.* **1998**, *69*, 2427.
- (28) Dion, M.; Ganne, M.; Tournoux, M. *Mater. Res. Bull.* **1981**, *16*, 1429.
- (29) Chen, Y.; Zhao, X.; Ma, H.; Ma, S.; Huang, G.; Makita, Y.; Bai, X.; Yang, X. *J. Solid State Chem.* **2008**, *181*, 1684.
- (30) Hata, H.; Kobayashi, Y.; Bojan, V.; Youngblood, W. J.; Mallouk, T. E. *Nano Lett.* **2008**, *8*, 794.
- (31) Ma, R.; Kobayashi, Y.; Youngblood, W. J.; Mallouk, T. E. *J. Mater. Chem.* **2008**, *18*, 5982.
- (32) Zhao, Y.; Vargas-Barbosa, N. M.; Strayer, M. E.; McCool, N.; Pandelia, M.-E.; Saunders, T.; Swierk, J.; Callejas, J.; Jensen, L.; Mallouk, T. E. *J. Am. Chem. Soc.* **2015**, *137*, 9.
- (33) Kresse, G.; Furthmüller, J. *Comput. Mater. Sci.* **1996**, *6*, 15.
- (34) Kresse, G.; Furthmüller, J. *Phys. Rev. B* **1996**, *54*, 11169.
- (35) Perdew, J. P.; Chevary, J. A.; Vosko, S. H.; Jackson, K. A.; Pederson, M. R.; Singh, D. J.; Fiolhais, C. *Phys. Rev. B* **1992**, *46*, 6671.
- (36) Kresse, G.; Joubert, D. *Phys. Rev. B* **1999**, *59*, 1758.
- (37) Monkhorst, H. J.; Pack, J. D. *Phys. Rev. B* **1976**, *13*, 5188 LP
- (38) Bader, R. F. W. *Accounts of Chemical Research* **1985**, *18*, 9.
- (39) Henkelman, G.; Arnaldsson, A.; Jonsson, H. *Comput. Mater. Sci.* **2006**, *36*, 354.
- (40) Zhao, Y.; Hernandez-Pagan, E. A.; Vargas-Barbosa, N. M.; Dysart, J. L.; Mallouk, T. E. *The Journal of Physical Chemistry Letters* **2011**, *2*, 402.
- (41) Rozanska, X.; Delbecq, F.; Sautet, P. *Physical Chemistry Chemical Physics* **2010**, *12*, 14930.
- (42) Brewer, L. *Acta Metall.* **1967**, *15*, 553.
- (43) Wang, H.; Carter, E. A. *J. Am. Chem. Soc.* **1993**, *115*, 2357.
- (44) Campbell, R. A.; Rodriguez, J. A.; Goodman, D. W. *Surface Science* **1990**, *240*, 71.
- (45) Rodriguez, J. A.; Campbell, R. A.; Goodman, D. W. *Journal of Physical Chemistry* **1991**, *95*, 5716.
- (46) Rodriguez, J. A.; Goodman, D. W. *Journal of Physical Chemistry* **1991**, *95*, 4196.
- (47) Heitzinger, J. M.; Gebhard, S. C.; Koel, B. E. *Surface Science* **1992**, *275*, 209.

Insert Table of Contents artwork here



Charge Transfer Stabilization of Late Transition Metal Oxide Nanoparticles on a Layered Niobate Support

Megan E. Strayer¹, Thomas P. Senftle², Jonathan P. Winterstein³, Nella M. Vargas-Barbosa¹, Renu Sharma³, Robert M. Rioux,^{1,2} Michael J. Janik^{*2}, and Thomas E. Mallouk^{*1}

¹Department of Chemistry, Physics and Biochemistry and Molecular Biology and ²Department of Chemical Engineering, The Pennsylvania State University, University Park, Pennsylvania 16802, United States

³Center for Nanoscale Science and Technology, National Institute of Standards and Technology, Gaithersburg, Maryland 20899, United States

Supplemental information (18 pp.)

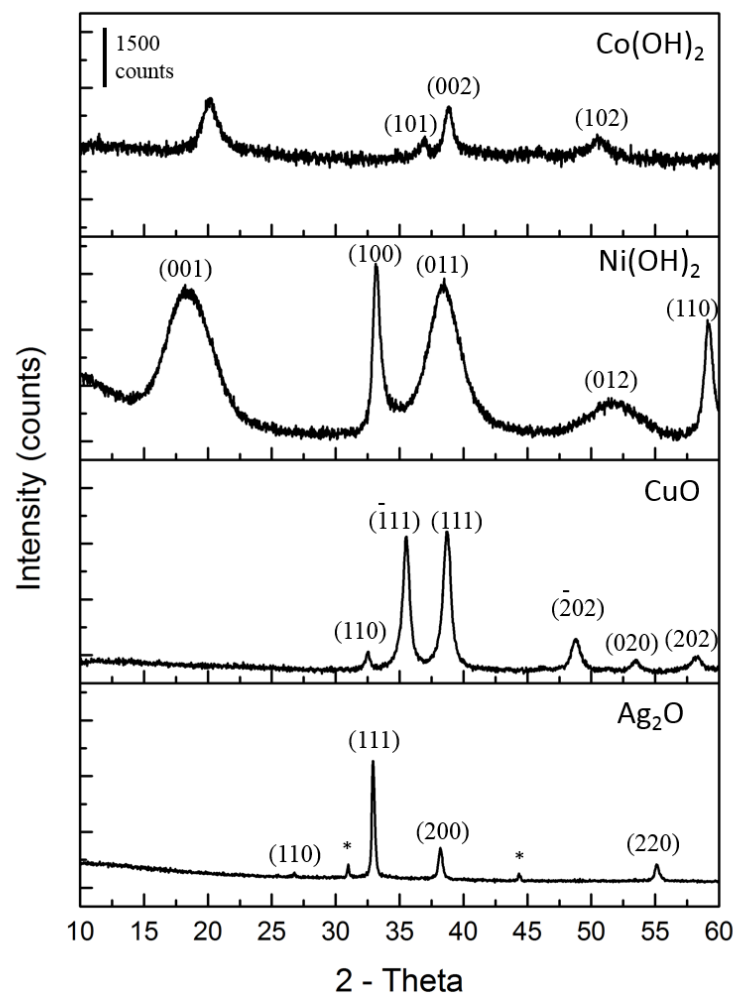


Figure S1. X-ray powder diffraction patterns of deposited nanoparticles. Metal halide precursors (CoBr₂, NiSO₄·6H₂O, CuSO₄, AgNO₃) were hydrolyzed in TBA⁺OH⁻ for 18 hours, and the precipitate was taken for analysis. For Ag₂O, an impurity peak at 31° 2-theta and a peak for Ag metal at 45° 2-theta are observed.

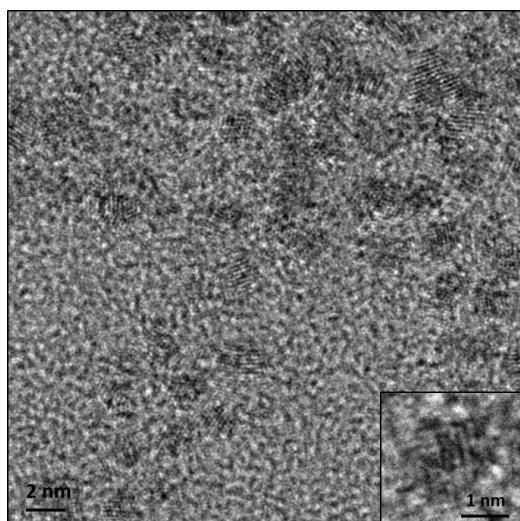


Figure S2. TEM of pre-formed, crystalline iridium hydroxide-capped $\text{IrO}_x \cdot n\text{H}_2\text{O}$ nanoparticles. The average diameter of the nanoparticles is $1.2 \text{ nm} \pm 0.3 \text{ nm}$ ($n = 299$).

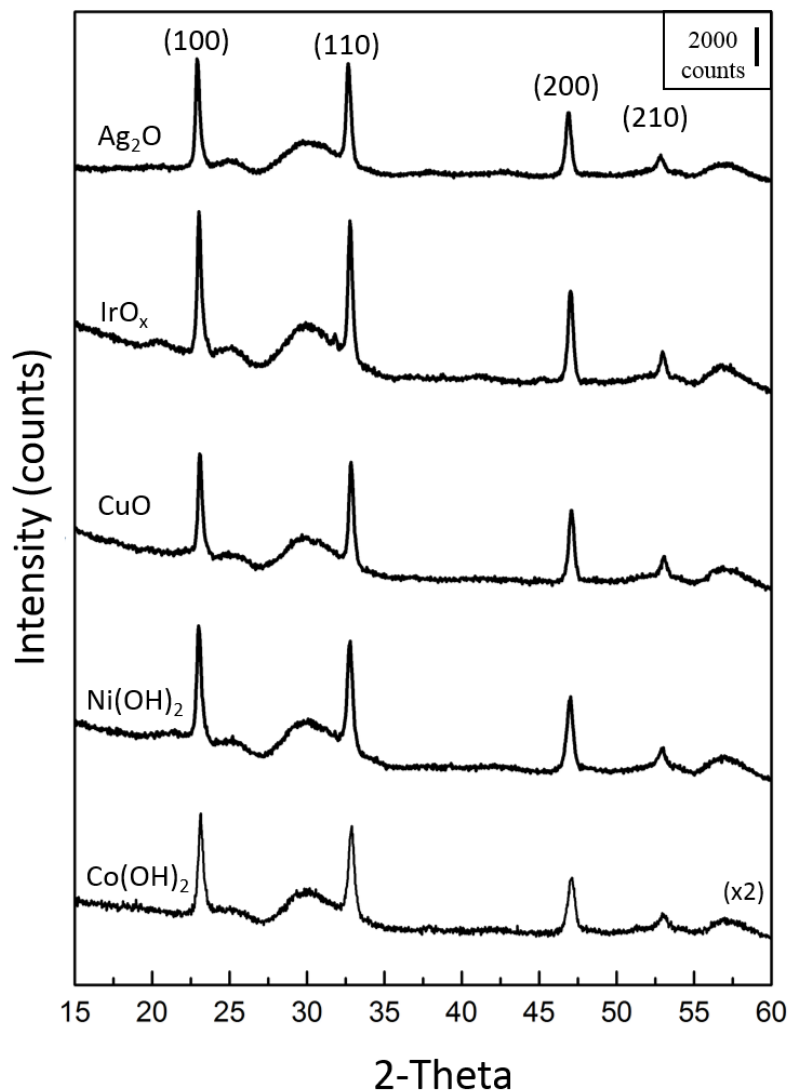


Figure S3. X-ray diffraction patterns of Co(OH)_2 , Ni(OH)_2 , CuO , iridium hydroxide-capped $\text{IrO}_x \cdot n\text{H}_2\text{O}$ and Ag_2O deposited onto nanosheets of $\text{TBA}_{0.24}\text{H}_{0.76}\text{Ca}_2\text{Nb}_3\text{O}_{10}$ then restacked with KOH . The intensities for Co(OH)_2 are multiplied by 2.

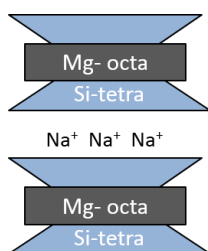


Figure S4. Na-TSM structure. Na-TSM is a T-O-T layered silicate with Na^+ in the interlayer galleries. This structure has no free surface Si-OH groups at the basal planes.

Measurement of reaction enthalpies from ITC data

Isothermal titration calorimetry (ITC) was used to determine the enthalpy change (ΔH) of metal nanoparticles interacting with oxide supports. In a classic ITC experiment, the equilibrium constant for binding (K), ΔH and n can be determined from the ITC thermogram because both the products and reactants are in considerable concentrations at equilibrium. Due to the complexity of the experiments performed in this report, only ΔH can be determined accurately from the ITC thermogram. Because of the numerous reactions occurring simultaneously during the nanoparticle deposition, not all reactants and products are in equilibrium for each of the individual reactions shown in Scheme 1 (main text). This does not allow for accurate measurements of n and K to be retrieved from the ITC data for the heat of interaction between nanoparticle and support.

In the ITC experiments, aliquots of the titrant solution (metal oxide/hydroxide precursor) were injected into a cell containing the oxide support, and the heat flow for each injection was recorded. Assuming that all the metal nanoparticles deposited onto the support, each heat flow was integrated to give the differential heat production (kJ mol^{-1}) per injection. Each integrated peak gives an independent ΔH value for the overall ITC reaction.

In the case of these experiments, an enthalpy screen was performed. For each ITC experiment, the concentrations of both the titrant and the cell solutions were varied to find conditions under which the first few injections produced constant ΔH values. At the concentrations where consecutive injections produced the same heat, it was assumed that all the nanoparticles for a single injection deposit onto the support and contribute to the heat of interaction. As the experiment continued, a sigmoid began to form, with smaller heats being produced with each consecutive injection. The smaller heats can be attributed to fewer nanoparticles binding to the support with each injection as the surface is covered with nanoparticles. Since ΔH is the only thermodynamic parameter we are able to extrapolate from these ITC experiments, the consistent enthalpy changes at the beginning of the sigmoid were used to obtain ΔH for the overall reaction.

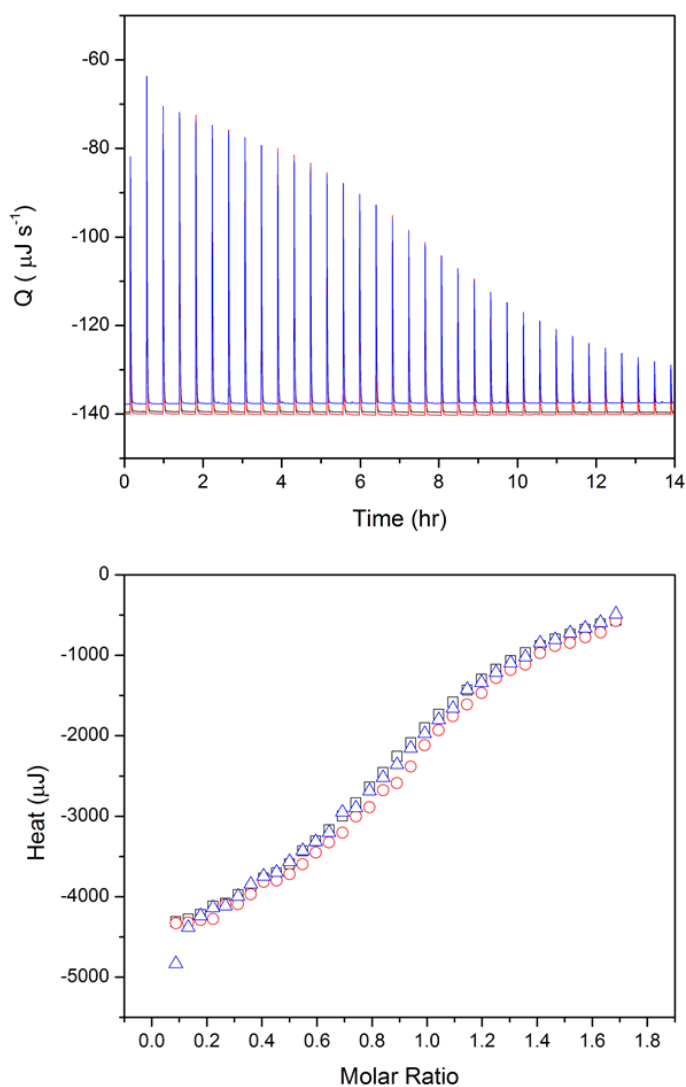


Figure S5. A) Real ITC thermograms for triplicate measurements of the addition of monomeric iridium anions ($[\text{Ir}(\text{OH})_5(\text{H}_2\text{O})]^{2-}$ and $[\text{Ir}(\text{OH})_6]^{2-}$) to $\text{TBA}_{0.24}\text{H}_{0.76}\text{Ca}_2\text{Nb}_3\text{O}_{10}$ nanosheets in excess TBA^+OH^- solution and B) the integrated heat data for of the triplicate thermograms shown in (A). These “raw” data show the precision of the data produced from different ITC experiments of the same sample.

In situ HRTEM and HAADF STEM experiments were performed in order to explore the correlation between interfacial bonding strength and thermally driven growth of nanoparticles. It is presumed that some reduction of the metal oxide/hydroxide nanoparticles occurs while heating in vacuum, although the extent of reduction is unknown. Our previous study of Rh(OH)₃ nanoparticles showed that the exothermic enthalpy of binding to different supports correlated with the resistance to particle growth in both vacuum and reducing atmospheres.²⁶ Additionally, density functional theory calculations (see main text) show that the bonding strengths of metals qualitatively follows the same trend as the metal oxide. Therefore, trends in the growth of nanoparticles are expected to be similar for oxide-supported metal oxide/hydroxides and metal nanoparticles.

Hydroxyiridate-capped IrO_x·nH₂O nanoparticles were deposited onto TBA_{0.24}H_{0.76}Ca₂Nb₃O₁₀, the sheets were restacked with KOH, and the samples were heated in vacuum. The diameter of the nanoparticles remains below 2 nm up to 1000 °C, although more nanoparticles are observable at higher temperatures. Both IrO_x·nH₂O nanoparticles and iridium(III) monomeric anions are present during nanoparticle deposition. The iridium monomer is known to strongly bind to and cover the surface of TiO₂,³² and its highly exothermic heat of interaction with the niobium oxide support has been measured in this work. Therefore, it is likely that the [Ir(OH)₅(H₂O)]²⁻ monomer covers most of the surface of the niobate nanosheets, and there is agglomeration of monomers that leads to the appearance of newly formed nanoparticles at high temperatures. The statistically insignificant growth of nanoparticles from room temperature to 1000 °C correlates with the strong heat of interaction between the [Ir(OH)₅(H₂O)]²⁻ monomer and the niobium oxide support ((-83 ± 17) kJ·mol⁻¹).

The sintering of Ag₂O nanoparticles on niobate nanosheets was also investigated. The heat of interaction between Ag₂O and the nanosheets was weakly endothermic ((6 ± 7) kJ·mol⁻¹). As the temperature is increased from 25 °C to 200 °C, the average diameter of the nanoparticles increases, and then remains the same between 200 °C and 600 °C, although the size distribution broadens. During heating, silver is likely being reduced, although the extent of reduction is not known. When the temperature was held steady at 700 °C, the nanoparticles decreased in size and eventually disappeared from some areas of the support. After cooling the sample, the particles returned to the surface of the nanosheets. Previous reports have shown that Ag⁺ can be readily exchanged for cations in layered oxide materials.⁴⁸⁻⁵⁰ Therefore, it is possible that Ag₂O or Ag nanoparticles are transforming (via rapid diffusion of Ag⁺) to silver ions in the niobium oxide host lattice at higher temperatures. The HAADF STEM images in Figure 4E,F show an area of the support where the nanoparticles grow from room temperature to 700 °C.

Hydroxyiridate-capped IrO_x·nH₂O and Ni(OH)₂ nanoparticles were deposited onto Na-TSM and heated *in situ* in the TEM. As noted in the main text, the average diameter of as-deposited hydroxyiridate-capped IrO_x·nH₂O and Ni(OH)₂ particles are larger on Na-TSM than on KCa₂Nb₃O₁₀. In both cases, the nanoparticles grow to larger diameters at lower temperatures than they do when they are deposited onto KCa₂Nb₃O₁₀. Figure S6A-B compares HAADF STEM images of Ni(OH)₂ on KCa₂Nb₃O₁₀ and Na-TSM heated to 600 °C. Ni(OH)₂ particles on KCa₂Nb₃O₁₀ are smaller than on Na-TSM at this temperature ((3.6 ± 0.9) nm (n = 59) versus (6 ± 3) nm (n = 107)), as well as more evenly distributed on the support. There are areas of the Na-TSM surface that are not covered by any Ni(OH)₂ particles. While the contrast is not as dramatic, the hydroxyiridate-capped IrO_x·nH₂O nanoparticles also grow more rapidly on Na-TSM ((1.8 ± 0.7) nm (n = 67)) than they do on KCa₂Nb₃O₁₀ ((1.1 ± 0.3) nm (n = 237)), and they do not cover the Na-TSM support evenly (Figure S6C-D). These data confirm the hypothesis that the weaker bonding interactions between the nanoparticles and silica-based supports are less effective in inhibiting nanoparticle growth than the stronger interactions with KCa₂Nb₃O₁₀.

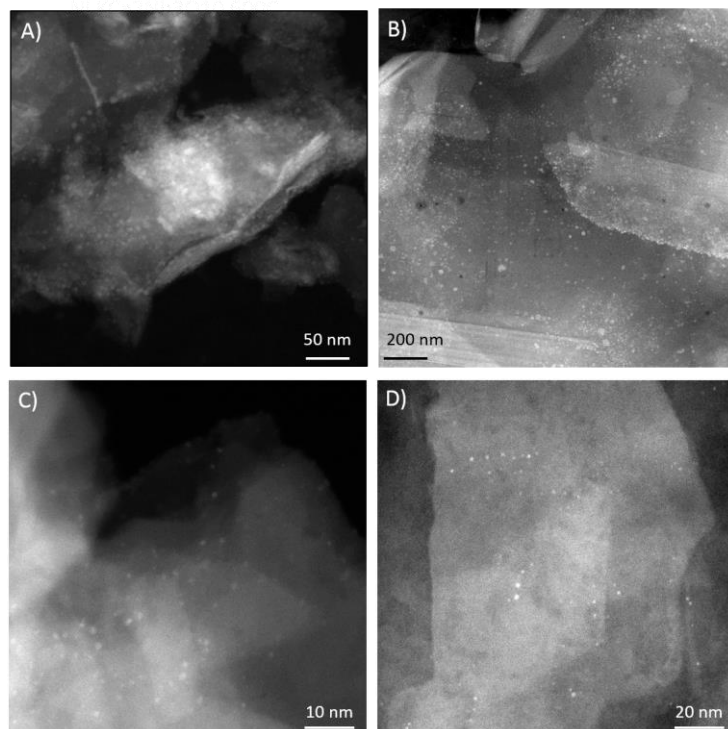


Figure S6. HAADF STEM images at 600 °C of Ni(OH)₂ on A) KCa₂Nb₃O₁₀ and B) Na-TSM and iridium hydroxide-capped IrO_x·nH₂O on C) KCa₂Nb₃O₁₀ and D) Na-TSM. Notice in B, the scale bar is quadrupled relative to A. In both cases, the nanoparticles deposited onto Na-TSM (right column) are unevenly distributed on the support and are larger than those deposited on KCa₂Nb₃O₁₀ (left column).

Table S1. Metal precursors used to deposit the corresponding metal oxide/hydroxide onto nanosheets. The lattice constants for the metal nanocrystals are also reported. Uncertainties are one standard deviation calculated from three measurements.

Metal Precursor	Metal nanoparticle	Lattice constants		
		a (nm)	b (nm)	c (nm)
CoBr ₂	Co(OH) ₂	0.332822(464)	0.332822(464)	0.463127(353)
NiSO ₄ ·6H ₂ O	Ni(OH) ₂	0.30675(756)	0.30675(756)	0.465495(2179)
CuSO ₄	CuO	0.469361(79)	0.342894(77)	0.513233(764)
AgNO ₃	Ag ₂ O	0.470983(18)	0.470983(18)	0.470983(18)

Table S2. Heats of formation for oxides (ΔH_f) and heats of sublimation for metals (ΔH_{sub}) used to determine $[\Delta H_{sub} - \Delta H_f]$ values for each metal. All values are obtained from Campbell *et al.*⁵ unless otherwise noted, and are reported here in kJ mol⁻¹ of metal atom.

Metal	ΔH_{sub}	ΔH_f	$[\Delta H_{sub} - \Delta H_f]$
Co ⁵¹	426.64	-297.30	722.97
Rh ⁵¹	555.98	-100.39	681.47
Ir ⁵¹	670.85	-274.13	945.95
Ni	431.47	-245.17	675.68
Pd	377.41	-85.91	462.36
Pt	565.64	-54.05	619.69
Cu	337.84	-167.95	506.76
Ag	284.75	-15.44	300.19
Au	367.76	9.65	358.11

Table S3. Number of measurements (n) reported for each value represented in Figure 4.

Temperature (°C)	IrO _x · n H ₂ O	Ag ₂ O
25	151	216
200	208	201
400	196	253
450	210	300
500	212	325
550	272	N/A
600	237	226
650	287	N/A
700	293	N/A
750	200	N/A
800	240	N/A
900	233	N/A
1000	243	N/A

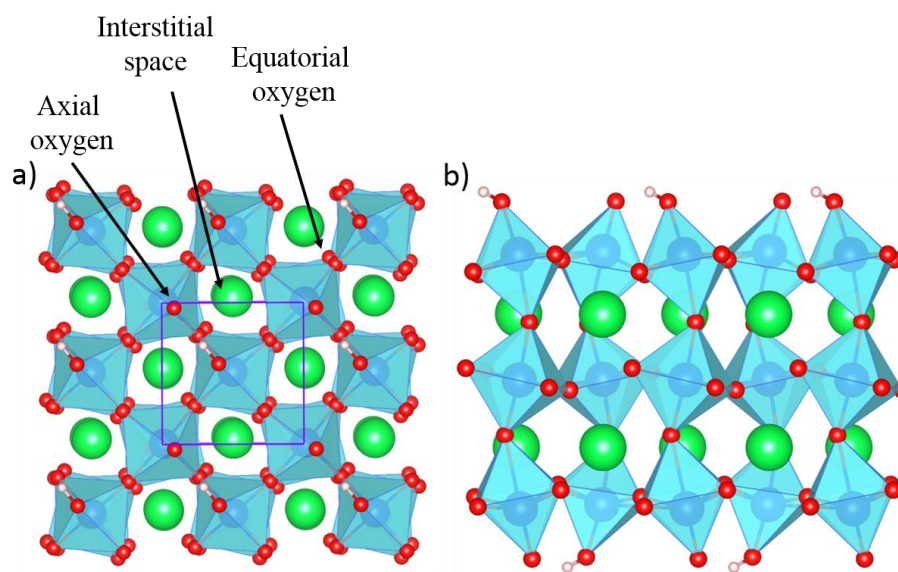


Figure S7. (a) Top and (b) side view of the HCa₂Nb₃O₁₀ surface model used in DFT binding energy calculations. Blue spheres are Nb, red spheres are O, green spheres are Ca, and white sphere are H. (a) shows the three possible surface binding sites of metal atoms and clusters to HCa₂Nb₃O₁₀: (1) axial oxygen, (2) equatorial oxygen, and (3) interstitial space between BO₆ polyhedra. Ca atoms are green, O atoms are red, Nb atoms are blue and H atoms are white.

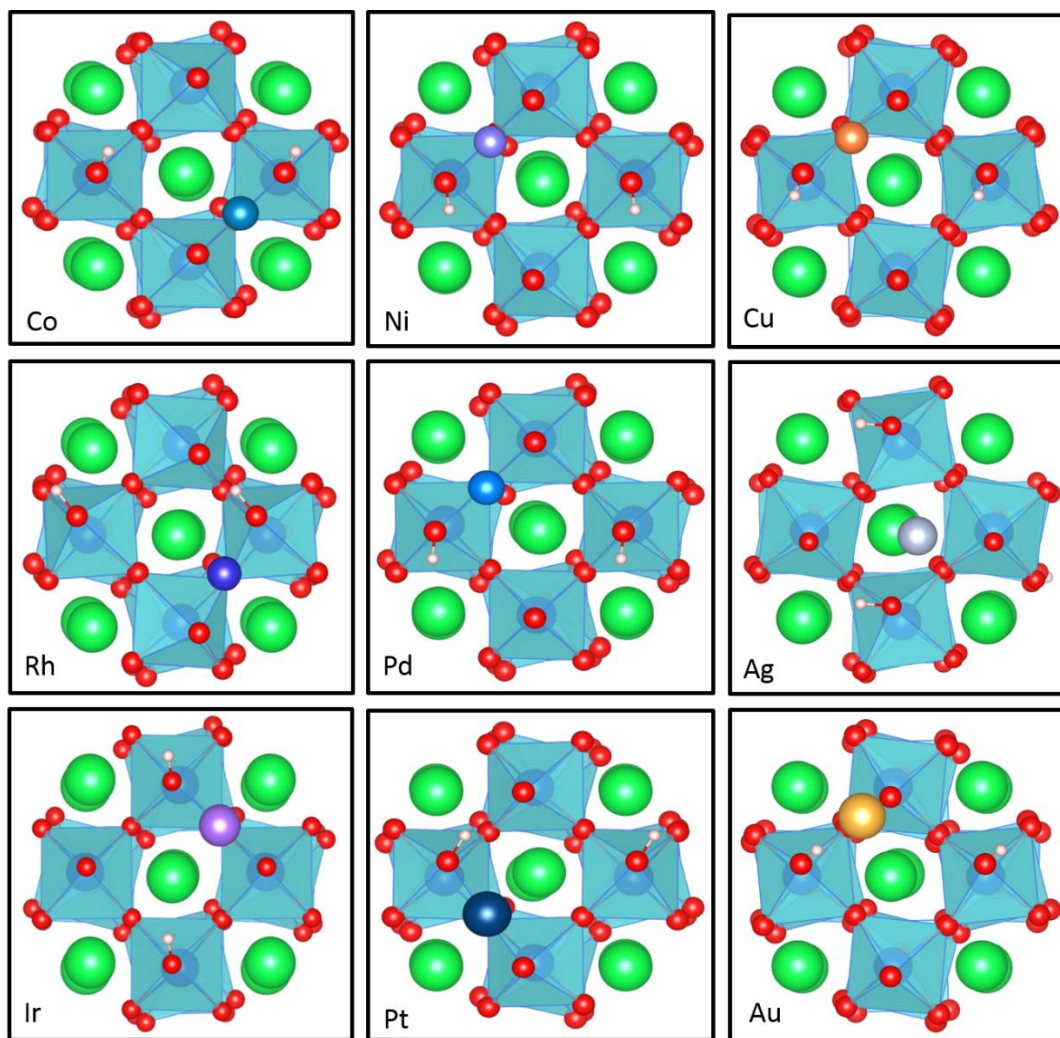


Figure S8. Optimized single atom adsorption geometries on the $\text{HCa}_2\text{Nb}_3\text{O}_{10}$ surface. Bond distances are provided in Table S3.

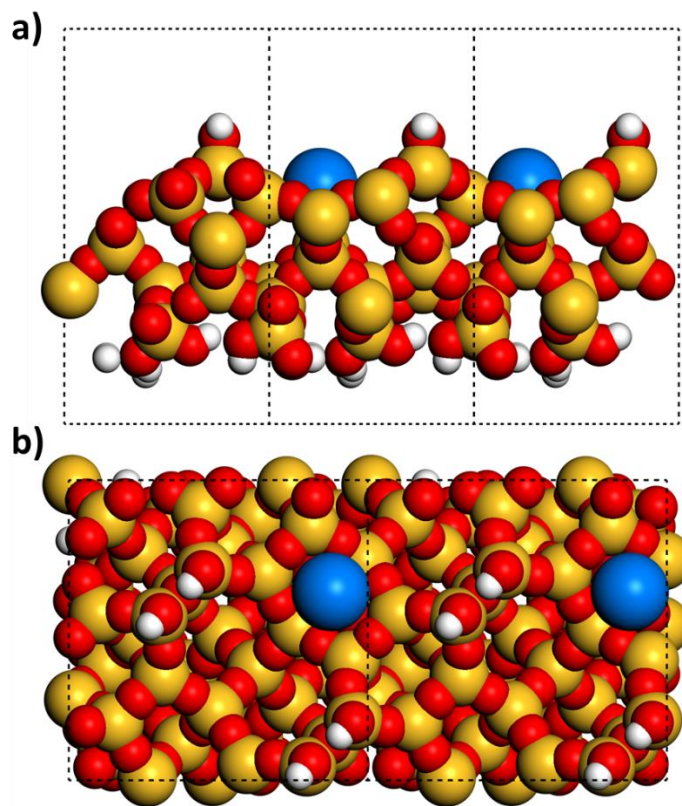


Figure S9. (a) Side and (b) top-down view of the optimized metal adsorption site on the SiO₂(001) model surface. The same adsorption site was used for all metals in this study.

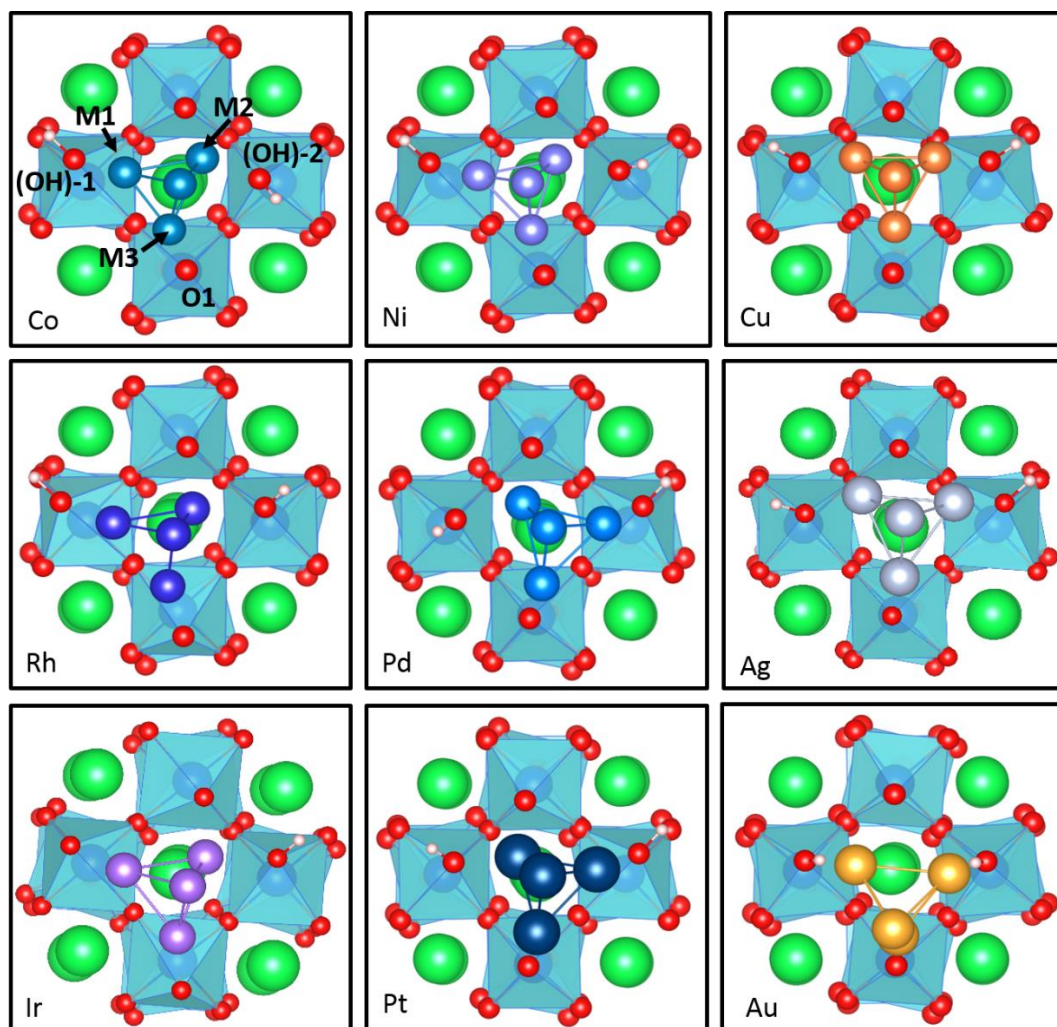


Figure S10. Optimized M_4 cluster adsorption geometries on the $\text{HCa}_2\text{Nb}_3\text{O}_{10}$ surface. Bond distances are provided in Table S2.

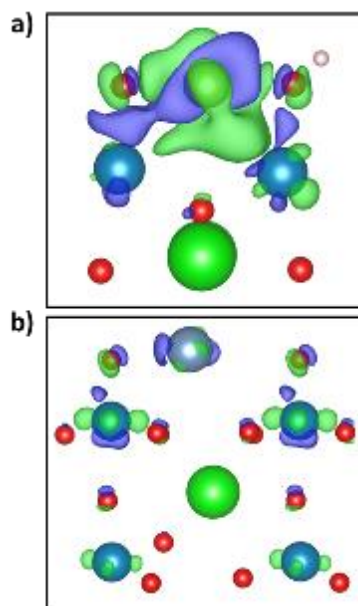


Figure S11. 3D charge density difference isosurfaces for (a) Ir and (b) Ag binding on the HCa₂Nb₃O₁₀ (001) surface. Valence electron charge accumulation is indicated by a green isosurface. The accumulation and depletion isosurfaces are shown at electron densities of $\pm 0.4 \text{ nm}^{-1}$.

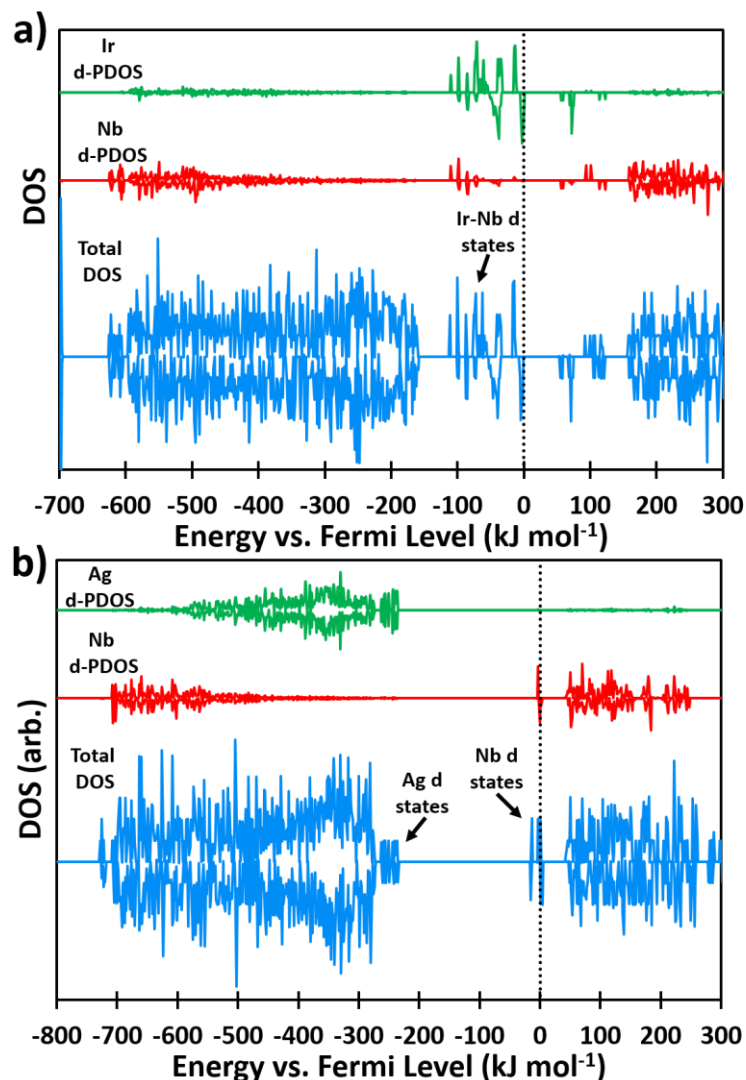


Figure S12. Total and partial density of states plotted relative to the Fermi level for HCa₂Nb₃O₁₀ supported (a) Ir and (b) Ag single atoms. The total DOS is shown in blue, the PDOS projected on the d states of the Nb surface atom adjacent to the adsorbed metal atom is shown in red, and PDOS projected on the d states of the adsorbed metal atom is shown in green. Spin up and spin down states are plotted on the positive and negative axes, respectively. The Fermi level is denoted by the vertical dotted line.

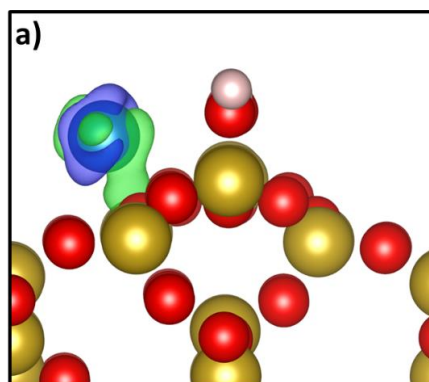


Figure S13. 3D charge density difference plots for Ir binding on the SiO₂ surface. The green (purple) isosurface reflects negative charge accumulation (depletion). The accumulation and depletion isosurfaces are shown at electron densities of $\pm 0.4 \text{ nm}^{-1}$.

Table S4. Calculated bond distance between adsorbed metal atom and closest O atom or (OH) group [nm].

Metal	M/O	M/(OH)
Co	0.180	0.182
Rh	0.200	0.203
Ir	0.191	0.199
Ni	0.181	0.184
Pd	0.203	0.205
Pt	0.199	0.203
Cu	0.182	0.185
Ag	0.230	0.231
Au	0.217	0.308

Table S5. Calculated bond distance between adsorbed metal cluster atoms and closest O atom or (OH) groups [nm]. (See Figure S9 for atom labeling scheme)

Metal	M3/O1	M1/(OH)-1	M2/(OH)-2
Co	0.185	0.189	0.201
Rh	0.197	0.204	0.225
Ir	0.191	0.195	0.220
Ni	0.184	0.189	0.209
Pd	0.210	0.243	0.220
Pt	0.201	0.215	0.211
Cu	0.186	0.196	0.195
Ag	0.212	0.225	0.218
Au	0.206	0.327	0.323

Table S6. Bader charge differences, in e , for metal binding on HCa₂Nb₃O₁₀ and SiO₂. Positive values indicate charge transfer from the late transition metal atom to the niobium atom in the support.

Metal	HCa ₂ Nb ₃ O ₁₀	SiO ₂
Co	+0.57	+0.08
Rh	+0.37	+0.06
Ir	+0.40	-0.13
Ni	+0.51	-0.18
Pd	+0.27	+0.07
Pt	+0.20	-0.01

Cu	+0.68	+0.05
Ag	+0.68	+0.05
Au	+0.09	+0.01

References:

- (1) Goodman, D. W. *Chem. Rev.* **1995**, *95*, 523.
- (2) Haruta, M. *Catal. Today* **1997**, *36*, 153.
- (3) Shekhar, M.; Wang, J.; Lee, W.-S.; Williams, W. D.; Kim, S. M.; Stach, E. A.; Miller, J. T.; Delgass, W. N.; Ribeiro, F. H. *J. Am. Chem. Soc.* **2012**, *134*, 4700.
- (4) Campbell, C. T. *Acc. Chem. Res.* **2013**, *46*, 1712.
- (5) Campbell, C. T.; Sellers, J. R. V. *Faraday Discuss.* **2013**, *162*, 9.
- (6) Cargnello, M.; Doan-Nguyen, V. V. T.; Gordon, T. R.; Diaz, R. E.; Stach, E. A.; Gorte, R. J.; Fornasiero, P.; Murray, C. B. *Science* **2013**, *341*, 771.
- (7) Valden, M.; Lai, X.; Goodman, D. W. *Science* **1998**, *281*, 1647.
- (8) Vayssilov, G. N.; Lykhach, Y.; Migani, A.; Staudt, T.; Petrova, G. P.; Tsud, N.; Skála, T.; Bruix, A.; Illas, F.; Prince, K. C.; Matolín, V. r.; Neyman, K. M.; Libuda, J. *Nat Mater* **2011**, *10*, 310.
- (9) Mostafa, S.; Behafarid, F.; Croy, J. R.; Ono, L. K.; Li, L.; Yang, J. C.; Frenkel, A. I.; Cuenya, B. R. *J. Am. Chem. Soc.* **2010**, *132*, 15714.
- (10) Haruta, M. *CATTECH* **2002**, *6*, 102.
- (11) Bonanni, S.; Aït-Mansour, K.; Harbich, W.; Brune, H. *J. Am. Chem. Soc.* **2012**, *134*, 3445.
- (12) Hu, Z.; Nakamura, H.; Kunimori, K.; Asano, H.; Uchijima, T. *J. Catal.* **1988**, *112*, 478.
- (13) Tauster, S. J. *Acc. Chem. Res.* **1987**, *20*, 389.
- (14) Tauster, S. J.; Fung, S. C.; Baker, R. T. K.; Horsley, J. A. *Science* **1981**, *211*, 1121.
- (15) Wang, Y.-G.; Yoon, Y.; Glezakou, V.-A.; Li, J.; Rousseau, R. *J. Am. Chem. Soc.* **2013**, *135*, 10673.
- (16) Meyer, R.; Ge, Q.; Lockemeyer, J.; Yeates, R.; Lemanski, M.; Reinalda, D.; Neurock, M. *Surface Science* **2007**, *601*, 134.
- (17) Addou, R.; Senftle, T. P.; O'Connor, N.; Janik, M. J.; van Duin, A. C. T.; Batzill, M. *ACS Nano* **2014**, *8*, 6321.
- (18) Negreiros, F. R.; Fabris, S. *The Journal of Physical Chemistry C* **2014**, *118*, 21014.
- (19) Vilhelmsen, L. B.; Hammer, B. *Physical Review Letters* **2012**, *108*, 126101.
- (20) Bruix, A.; Lykhach, Y.; Matolínová, I.; Neitzel, A.; Skála, T.; Tsud, N.; Vorokhta, M.; Stetsovych, V.; Ševčíková, K.; Mysliveček, J.; Fiala, R.; Václavů, M.; Prince, K. C.; Bruyère, S.; Potin, V.; Illas, F.; Matolín, V.; Libuda, J.; Neyman, K. M. *Angewandte Chemie International Edition* **2014**, *53*, 10525.
- (21) Hansen, T. W.; DeLaRiva, A. T.; Challa, S. R.; Datye, A. K. *Accounts of Chemical Research* **2013**, *46*, 1720.
- (22) Fu, Q.; Yang, F.; Bao, X. *Acc. Chem. Res.* **2013**, *46*, 1692.
- (23) Hansen, P. L.; Wagner, J. B.; Helveg, S.; Rostrup-Nielsen, J. R.; Clausen, B. S.; Topsøe, H. *Science* **2002**, *295*, 2053.
- (24) Campbell, C. T.; Parker, S. C.; Starr, D. E. *Science* **2002**, *298*, 811.
- (25) Prieto, G.; Zečević, J.; Friedrich, H.; de Jong, K. P.; de Jongh, P. E. *Nat Mater* **2013**, *12*, 34.

- (26) Strayer, M. E.; Binz, J. M.; Tanase, M.; Kamali Shahri, S. M.; Sharma, R.; Rioux, R. M.; Mallouk, T. E. *J. Am. Chem. Soc.* **2014**, *136*, 5687.
- (27) Stuckless, J. T.; Frei, N. A.; Campbell, C. T. *Rev. Sci. Instrum.* **1998**, *69*, 2427.
- (28) Dion, M.; Ganne, M.; Tournoux, M. *Mater. Res. Bull.* **1981**, *16*, 1429.
- (29) Chen, Y.; Zhao, X.; Ma, H.; Ma, S.; Huang, G.; Makita, Y.; Bai, X.; Yang, X. *J. Solid State Chem.* **2008**, *181*, 1684.
- (30) Hata, H.; Kobayashi, Y.; Bojan, V.; Youngblood, W. J.; Mallouk, T. E. *Nano Lett.* **2008**, *8*, 794.
- (31) Ma, R.; Kobayashi, Y.; Youngblood, W. J.; Mallouk, T. E. *J. Mater. Chem.* **2008**, *18*, 5982.
- (32) Zhao, Y.; Vargas-Barbosa, N. M.; Strayer, M. E.; McCool, N.; Pandelia, M.-E.; Saunders, T.; Swierk, J.; Callejas, J.; Jensen, L.; Mallouk, T. E. *J. Am. Chem. Soc.* **2015**, *137*, 9.
- (33) Kresse, G.; Furthmuller, J. *Comput. Mater. Sci.* **1996**, *6*, 15.
- (34) Kresse, G.; Furthmuller, J. *Phys. Rev. B* **1996**, *54*, 11169.
- (35) Perdew, J. P.; Chevary, J. A.; Vosko, S. H.; Jackson, K. A.; Pederson, M. R.; Singh, D. J.; Fiolhais, C. *Phys. Rev. B* **1992**, *46*, 6671.
- (36) Kresse, G.; Joubert, D. *Phys. Rev. B* **1999**, *59*, 1758.
- (37) Monkhorst, H. J.; Pack, J. D. *Phys. Rev. B* **1976**, *13*, 5188 LP
- (38) Bader, R. F. W. *Accounts of Chemical Research* **1985**, *18*, 9.
- (39) Henkelman, G.; Arnaldsson, A.; Jonsson, H. *Comput. Mater. Sci.* **2006**, *36*, 354.
- (40) Zhao, Y.; Hernandez-Pagan, E. A.; Vargas-Barbosa, N. M.; Dysart, J. L.; Mallouk, T. E. *The Journal of Physical Chemistry Letters* **2011**, *2*, 402.
- (41) Rozanska, X.; Delbecq, F.; Sautet, P. *Physical Chemistry Chemical Physics* **2010**, *12*, 14930.
- (42) Brewer, L. *Acta Metall.* **1967**, *15*, 553.
- (43) Wang, H.; Carter, E. A. *J. Am. Chem. Soc.* **1993**, *115*, 2357.
- (44) Campbell, R. A.; Rodriguez, J. A.; Goodman, D. W. *Surface Science* **1990**, *240*, 71.
- (45) Rodriguez, J. A.; Campbell, R. A.; Goodman, D. W. *Journal of Physical Chemistry* **1991**, *95*, 5716.
- (46) Rodriguez, J. A.; Goodman, D. W. *Journal of Physical Chemistry* **1991**, *95*, 4196.
- (47) Heitzinger, J. M.; Gebhard, S. C.; Koel, B. E. *Surface Science* **1992**, *275*, 209.
- (48) Sato, M.; Watanabe, J.; Uematsu, K. *J. Solid State Chem.* **1993**, *107*, 460.
- (49) Boltersdorf, J.; Maggard, P. A. *ACS Catalysis* **2013**, *3*, 2547.
- (50) Toda, K.; Watanabe, J.; Sato, M. *Solid State Ionics* **1996**, *90*, 15.
- (51) *Handbook of Chemistry and Physics: A Ready Reference Book of Chemical and Physical Data*; 84 ed.; Lide, D. R., Ed.; CRC Press: New York, 2004.